Micro-Porosity of the Intervertebral Disc and Its Effects on Fluid Transport: A Scanning Electron Microscopy and Histological Study

by

Ross Robert Foster

B.S/M.S., University of Colorado, 2009

A thesis submitted to the

Faculty of the Graduate School of the

University of Colorado in partial fulfillment

of the requirements for the degree of

Master of Science

Department of Mechanical Engineering

2009

ProQuest LLC
789 East Eisenhower Parkway
P.O. Box 1346
Ann Arbor, MI 48106-1346

This thesis entitled:
Micro-Porosity of the Intervertebral Disc and
Its Effects on Fluid Transport:
A Scanning Electron Microscopy and Histological Approach
written by Ross R. Foster
has been approved for the Department of Mechanical Engineering

_____

Virginia Ferguson, PhD

_____

Franck Vernerey, PhD

Date: December 8, 2009

The final copy of this thesis has been examined by the signatories, and we find that both the content and the form meet acceptable presentation standards of scholarly work in the above mentioned discipline.

Foster, Ross Robert (M.S. Mechanical Engineering - Bioengineering)

Micro-Porosity of the Intervertebral Disc and Its Effects on Fluid Transport: A Scanning Electron Microscopy and Histological Approach

Thesis directed by Professor Virginia L. Ferguson, PhD

Abstract

The intervertebral disc (IVD) allows for mobility of the spine. Healthy function of the IVD relies on complex transport of nutrients, primarily through fluid mechanisms. However, current understanding of these fundamentals lacks observable experimental properties, such as porosity, which will greatly enhance both the mathematical descriptions and computational simulations of the anatomical region. This thesis establishes data for the rat IVD porosity and suggests a possible mathematical method for analyzing such data.

Research has shown that the material properties of the IVD plays an important role in healthy disc function. This thesis also examines the impact of changing porosity and on the fluid permeability of the cartilaginous endplate (CE). DDD affects most individuals in old age, and the costs of treating this disease are becoming ever more expensive as medicine continues to advance the life expectancy age. Understanding how the structures of the IVD remain intact throughout our lives will play an immensely important role in developing bioengineered materials, surgical techniques, and therapies for rehabilitation of DDD.

Porosity measurements were taken from the spines of healthy Sprague Dawley rats. Spines were dissected, dehydrated, and either prepared for SEM imaging or histological analysis. For SEM imaging, samples were processed according to different protocols and results compared. Overall porosity was Images showed a strong indication for a possible attachment mechanism between the CE and adjacent bone while additionally providing a secondary measurement system of porosity and anatomical surface features. Histological samples were fixed in polymethylmethacrylate (PMMA), sectioned across the middle of the

IVD sagitally, and stained for both quantitative porosity measurements and qualitative compositional observations. Results show ventral and dorsal differences within and cranial and caudal differences between the cartilaginous endplates of the IVD. Porosity was determined to be anisotropic with a radial dependence. Visible pore fractions ranged from 10-25% in the cranial CE and from 7-20% caudally, with both peaks approximately adjacent to the nucleus pulposus. The research presented in here and also in literature show that the as-measured state of dehydrated samples is not a true measure of porosity and needs to include intrafibrillar volumes. The cranial and caudal CE pore sizes were determined to increase proximally to distally from the spinal cord ranging from $1300\mu m^2$-$8900\mu m^2$ and from $520\mu m^2$-$870\mu m^2$ respectively. The cranial CE within a vertebral body unit had markedly larger pore distribution in the distal 40% than the caudal CE that had a relatively small pore distribution across the entire diameter. Visible pore fractions ranged from 9.4% to 25% in the cranial CE and from 7.9% to 18.4% in the caudal CE, both showing a radial dependence. The CE thickness also showed radial dependence for both top and bottom endplates with values ranging from .201mm-.548mm and .182mm-.319mm respectively, exhibiting a both an axial location and radial dependence. The pore fractions were greatest above and below the Nucleus Pulposus (NP) implying maximum flow in these regions and that cranial and caudal endplates have very different porosity characteristics.

Acknowledgements

I want to thank the staff at the Nanoscale Characterization Facility at the University of Colorado for their wonderful assistance with all of my SEM imaging. I want to thank Tom Giddings et al. from MCDB for use of their critical point dryer with my tissue preparation. I want to thank the students in the Mahoney group and Vikas Patel from Orthobiomechanics at the Anchutz Medical Center for helping me to acquire the all of the tissues used. I'd also like to thank the Anseth Lab for their assistance with my histology samples. I'd like to thank everyone in the Ferguson group, but I would especially like to thank Sara and Blair for their advice and assistance throughout. I want to thank Professor Vernerey for his assistance with the mathematics herein and for serving on my committee.

I would like to extend special acknowledgements to Ginger, my advisor, for the numerous hours of effort and patience she has had with me. Without her, none of this would have been possible. Thank you, Professor.

I would also like to thank my family and my girlfriend for their love and support throughout this process. Without you all, this would have been much more difficult.

This has been an invaluable life experience for me; the lessons are far beyond academic. Despite the relatively short duration, I have grown and changed in many ways for the better and I greatly appreciate the opportunity life has given.

Table of Contents

Table of Tables

Table of Figures

Table of Equations

1.0 - Introduction/Motivation

The human spine is responsible for many very important functions of the body. Primarily, the spine protects and nourishes the delicate spinal cord, and literally and figuratively forms the backbone of the trunk. Damage to the spine is incredibly detrimental to one's quality of life because of its inherent value to the healthy human body. Injury to any part of the spine can have a long-reaching impact, which is why so much money and so many researchers have dedicated themselves to the study of the spine.

Degeneration of the intervertebral disc (IVD) within the spine, publicly called DDD, is a condition that can be very painful for many individuals, so much so that the quality of life is greatly impacted. During degeneration, the IVD undergoes both morphological and biochemical changes that alter tissue hydration, permeability, and the load bearing capacity of the disc. IVD degeneration is associated with mechanical damage, loss of nutritional pathways, and biological degradation. Disc degeneration occurs with age, but can also occur with acute injury, as with lifting accidents. Degeneration is the process in which the IVD's water fraction decreases over long periods of time. As a result, the disc no longer has the capability to withstand the strong forces that the body imposes. Subsequently, the disc begins to break down significantly which decreases the disc's energy absorption and cushioning abilities. With degeneration, the discs in the spine dehydrate and lose their energy absorption and cushioning abilities. The disc can lose as much as 30% of water content with degeneration. The avascular nature of the disc further hinders the repair process, as nutrients and waste rely on good porosity and flow properties combined with appropriate loading and mechanical response for transport. Damage to any of these characteristics starts the process of degeneration that subsequently causes major loss of viscoelastic properties, fostering a positive feedback loop of damage to the IVD.

The main symptom of degeneration is pain; it occurs primarily in the lumbar region where degeneration is most common but is not limited to the region. Pain can also manifest itself in the hips, buttocks, neck, thighs, shoulders, arms, and even the hands. In these situations, typical physiological movements cause increased pain further limiting mobility in individuals with DDD. With injury comes inflammation, which aggravates adjacent nerves, increasing pain levels. Ultimately, disc degeneration can have long term and far reaching consequences, having a huge negative impact on an individual's quality of life.

The primary focus of research in the past has been on the disc itself but recent breakthroughs have begun to suggest that adjacent tissues, such as the cartilaginous endplate (CE), also have a strong influence on the mechanical properties of the region. The CE has been demonstrated to be a major controlling factor of fluid flow to the region and thus requires a great level of scrutiny. A preliminary investigation into basic principles should be able to describe the contribution of flow characteristics on mechanical properties. Information gained from this preliminary investigation will form a backbone for increasingly accurate models and simulations of fluid flow properties.

1.1 - Objectives of This Research

The true porosity of the IVD has had little experimental validation despite a relatively firm understanding of mechanical properties. Current modeling and literature rely on broad assumptions relating to homogeneity and the degree of anisotropy of porosity that have strong ramifications on resulting computer simulations. As a result, these assumptions cause compounding mathematical error within the equations that drive the simulations and can ultimately have disastrous consequences on final outcomes. Current simulations rely on two incorrect methodologies. One, the porosity is back solved from permeability measurements and is never measured directly. While ignoring porosity measurements may not necessarily matter for macroscopic mechanical properties, it cannot be ignored from a micro-scale standpoint because of the large impact of local changes. Even with local permeability constants, any fluid or viscoelastic inclusive simulation will never be completely accurate because the specific method of fluid transport is based on assumption rather than observation. Secondly, because of indirect measurement, the porosity of IVD tissues is assumed to be homogenous. Inhomogeneity is exhibited throughout the body and is therefore an strong indicator that current assumptions are incorrect. The aim of this research is to collect preliminary data to begin to correct for these errors and to attempt to describe what these observations entail.

The primary objective of this thesis is to establish pore size, fraction, distribution, and CE thickness in IVD tissue to provide a benchmark for studying the effects of degenerative disc disease (DDD). This will be accomplished via two aims. First, direct quantitative values of local pore number, size, and area fraction of the rat cartilaginous endplate. Second, this data will be used to develop a mathematical model that can describe permeability constants based on region. This new approach, combined with direct

measurements of the IVD, will enable location specific permeability constants to be predicted rather than the averaged values stated in literature.

2.0 - Background and Significance

The human intervertebral disc (IVD) has been studied extensively at the macroscopic level. Numerous finite element methods have been able to successfully model observed mechanical properties of the IVD.[10,12,14,26,33,36,38,39,45] However, despite their value, many of these types of methods make assumptions about the microstructure. Such methods can be improved with information regarding the material constituents at the micron level and their relationship to the observed mechanical properties, namely porosity. If the porosity of a structure increases, so does the permeability to fluids, and the permeability of the IVD has direct correlation to both acute and general damage. More specifically, degeneration of the disc combined with subsequent pain is a result of dehydration; i.e. lowered permeability. Many investigators have both experimentally and theoretically determined the permeability properties of the IVD.[1,2,4,12,15,19,20,31,42] The mathematics behind these models are quite complex, but the fundamental formulas rely on key constants that have not been measured before which implies a degree of inaccuracy in each of them.

2.1 - Anatomy

The IVD is located in between adjacent vertebrae in the spinal column. There are 23 discs in the human spine and the discs are identified most commonly by the vertebrae that the discs separate, i.e. L4-L5 for the disc between the lumbar vertebrae 4 and 5. The vertebrae and adjacent IVD provide primarily mechanical strength to the area by resisting the majority of compressive, tensile, and torsional loading throughout daily activities.[15,17,24] The IVDs, combined with ligaments and facet joints also allow for the mobility of the spine.[24] Broken down into its fundamentals, the disc is composed mainly of fibrocartilage, itself made primarily of proteoglycans and collagen fibers.[20,24,42] There are two defining regions within the disc; a central nucleus pulposus (NP) surrounded by the annulus fibrosus (AF), forming a

doughnut-like structure [Fig 1].[1,9,24,42] On the top and bottom of the disc lie cartilage endplates cranially and caudally.[5,12,24,42] Cranially and caudally to these are vertebrae made of bone [Fig 2].[5,12]

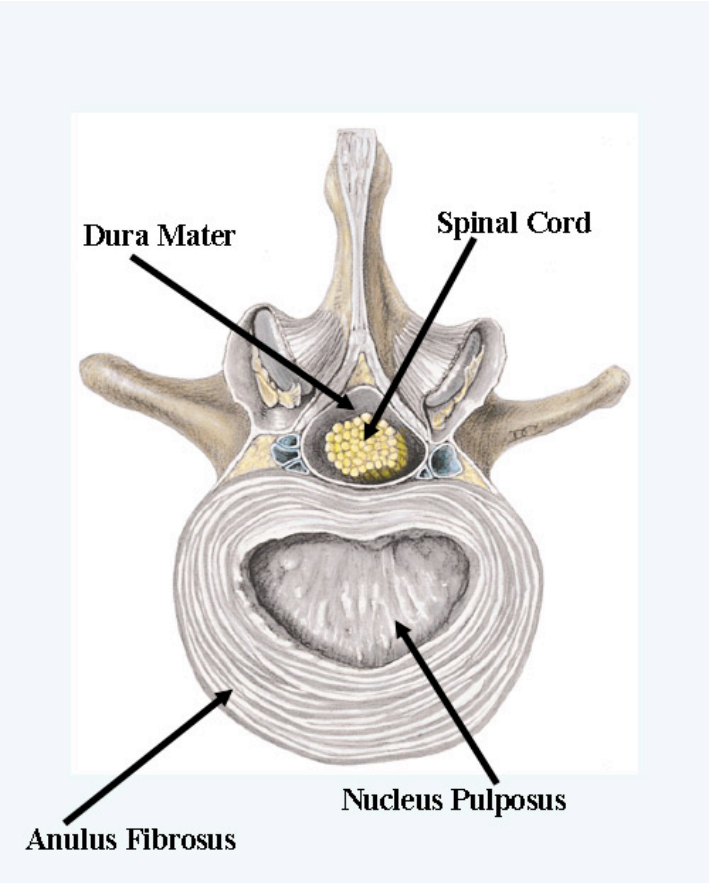

Figure 1 - Axial View of Spinal Unit
showing the cross-section of the intervertebral disc and the spinal cord. Note the layers of the annulus fibrosus and the jelly-like nucleus pulposus. Figure taken from Smith *et al*., 2005.[9]

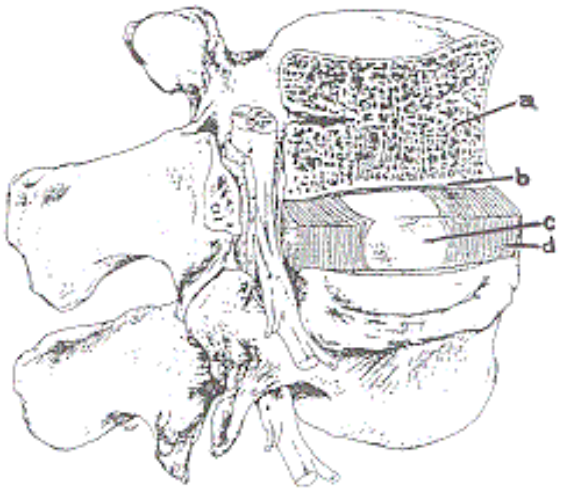

Figure 2 - Isometric View of Spinal Unit[25]
showing the a) vertebra, b)cartilaginous endplate, c)the nucleus pulposus, and d)the annulus fibrosus

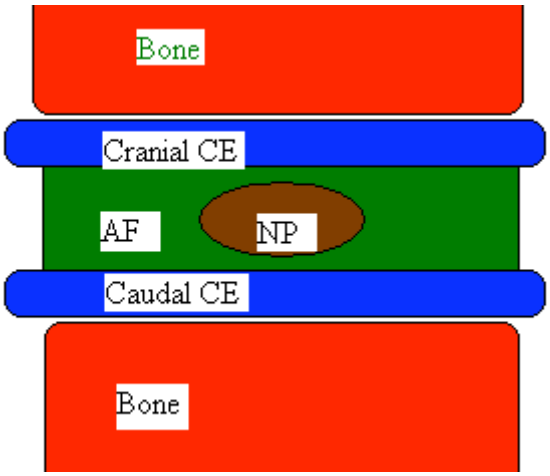

Figure 3 – Normal vertebral motion segment showing cartilaginous endplate (CE), annulus fibrosus (AF), and nucleus pulposus (NP) in typical spatial locations.

The unique mechanical properties of the IVD arise, like all materials, from both constituent content and spatial organization.[24,42] Being the largest avascular structure in the body, the extracellular matrix of the IVD is quite complex.[1,12,42] The primary function of the IVD is mechanical in nature, but also contributes to cell signaling and activity.[12,15] The NP's main function is to act like a shock absorber by dampening impacts.[17] The NP has a very

high water content that makes it a jelly-like substance due to high proteoglycan concentration.[1,17,20] Generally, the proteoglycan concentration is highest in the center of the IVD and has a decreasing gradient radially outward.[24] Conversely, the collagen concentration gradient is in the opposite direction, with the highest concentration within the outer AF.[24] Such a gradient means that the AF's primary function is mechanical functioning; to distribute the loads and pressures of the body onto the disc evenly.[4]

The nature of the transition zone between soft and stiff tissue requires complicated and difficult sample preparation techniques for histological examination and mechanical testing, increasing the difficulty in obtaining quality and reliable results.[20] Study of the region has received limited focus from scientists. The observations for the similar but different tissues to anchor to each other have been studied on a limited basis, but it appears as if the mechanisms behind these observations have not been examined at all. In this study, the complex surface topology appears to mechanically assist the structural region in the transition zone between the soft tissue of the IVD and the stiffer adjacent bone, but a full understanding of this phenomenon is still a mystery.

2.2 - Analogs

Oftentimes, political, ethical, or logistical constraints prevent the use of human IVD's for study. In these cases, it is important to determine if alternatives are available for study. Good analogs need to be utilized properly. Bovine discs are a common substitution because of large sample size.[17,31,46] Pig and dog samples have also been used with success.[4,20,42] Using geometrically larger samples allows for ease of extraction and simplifies experimental setups. Cost constraints and tissue availability commonly limit researchers' abilities to more expensive and difficult to obtain tissues, such as human cadaver tissue. Therefore, rat tissue has also been used extensively due to the cheap cost, high level of availability, and ease of controlled environmental conditions. Rat tissue is also commonly used due to the ability to

induce damage in order to study drug or treatment effects.[13] In addition, transgenic studies with rats have the ability to study gene effects on muscle, bone, and other tissue growth because of the rats' relatively close genetic nature to humans.[8,32] These studies show that rat tissue is a sufficient alternative to human tissue despite the small geometry.

2.3 - Sample Preparation

Electron microscopy and histological examination require imaging conditions that make sample preparation of highly hydrated tissues quite complex. To this end, researchers have tried many different approaches to achieving ideal conditions. Despite being numerous, sample preparation techniques tend to be similar and vary only within the following method steps: cutting or sectioning, drying, marking for content, and imaging apparatus. Careful selection of tissue type (species) and fixative procedures will increase quality yields and reduce potential sample distributions.

2.3.1 – SEM Imaging

Scanning electron microscopy (SEM) can draw strong conclusions about surface features of a sample. When applied to IVD tissues, SEM imaging provides valuable microstructural data;: information regarding fiber and fluid channel orientations, matrix constituents, and fiber densities. Collagen fiber orientation angles within the AF have been seen to change not only with radial direction, but also with circumferential direction.[18] In this thesis, it will first be important to establish that SEM imaging will have the capability to duplicate the above results as an important starting step for method verification.

Sample preparation for SEM imaging can be quite complex and has a large effect on subsequent results. Fixative materials and drying methods using graded ethanol series and/or CO_2 drying methods have been used and appear to generate qualitatively accurate results, but are insufficient for quantitative porosity measurments.[43] Liquid propane submersion

transferred to liquid nitrogen submersion followed by a freeze substitution process with liquid acetone also produces qualitatively excellent results with respect to porosity, but again fails at providing adequate quantitative data.[21] A third method presented in the literature includes fixing tissue with 2% gluteraldehyde in phosphate buffer solution (PBS), dried first in a graded ethanol series, and finally dried further with immersion in hexamethyldisilizane also producing good qualitative results.[42] These types of more advanced preparation methods represent a second step in improving the quality of resultant images for porosity measurements and many were attempted in this thesis in order to determine the best approach to obtaining quantitative porosity measurements.

For higher mineralized biomaterials, such as the vertebral endplate, removal of all adjacent low mineral content soft tissue is necessary in order to prevent blockage of pores and to increase image clarity. Depending on the accuracy required, simply physically removing the tissue may be enough for qualitative imaging. However, hypochloric acid may also be used to remove the low mineral tissue.[30] In this thesis, higher mineralized biomaterials were imaged and the alternative preparation methods were surveyed to determine the best protocol for the abovementioned tissue.

2.3.2 – Histology

Histology has also been used rather extensively to attempt to examine the composition of the IVD and vertebral endplate.[18,30,40] These studies have been limited to staining and optical imaging which is limited at maximum to 200 nm and can only resolve strongly refracting objects; both of which limit clarity as compared to SEM. Optical and confocal fluorescence imaging has also been used in an attempt to view collagen orientations and fiber densities with some success.[46] Yu et al. attempted to determine the network architecture of the extracellular matrix (ECM) but had a limited sample number. These limitations might suggest that histological approaches for IVD tissue should instead focus on

fractional composition of tissues. To this end, histological examination of composition showed microfibrillar network organizations showed large amounts of regional variation.[46] The changing network organization are the source of the variation of the mechanical properties of the IVD. Furthermore, Yu et al. suggest that the microfibrillar network in the annulus plays mainly a mechanical role while the network around the nucleus is mainly there for healthy cell function. Proteoglycan and water content distributions have been studied quite extensively, with the most detailed study being obtained in sagittal, coronal, and axial directions. As expected, both show strong concentrations from the center of the disc and decrease radially outward.[23]

The many different methods used throughout literature suggest sample preparation imparts a bias toward results by altering physical properties. Understanding how these different approaches affects results and then selecting a method to minimize undesirable effects is the key to obtaining quality samples. In order to determine the best preparation protocol for this thesis, many different approaches were surveyed for strengths and weaknesses based on desired results and the final selection was based primarily on the method's capability to provide reliable quantitative data.

2.4 - Mathematical Analysis

While experimental protocols are important in developing a solution for the microstructure, analysis of mechanical behavior cannot be ignored. For soft tissues, stresses and strains are difficult but straightforward to obtain. The more obscure selection is based on the constitutive equations used. Poroelasicity is a rather common choice and useful for the intervertebral disc, as well as viscoelasticity for creep measurements.[45] However, some have developed more complex osmoviscoelastic models based on experimental parameters determined and those found in literature.[38] Failure analysis is of high importance, because if the mechanisms of failure are well understood, then the effects are twofold. Prevention and

diagnostic methods can be developed that reflect these causes of failure and FE models can be adjusted to reflect these failure modes. The outcome of increased accuracy within FE models would be an overall increase quality of treatment. Therefore, understanding the mechanisms of fluid flow through the vertebral bodies becomes an important focus of research. A first step in this direction lies in understanding permeability.

2.5 - Permeability

Decreased permeability of the IVD is considered to be the major cause of degeneration.[3] When the permeability decreases, the cells of the disc can no longer receive appropriate nutrient and waste transport and will no longer be healthy.[2,3,5,17] Furthermore, decreased permeability leads to ECM degradation.[17] As a result, unchanging loading patterns on a weaker tissue will foster a positive feedback loop of damage. Therefore, the permeability of the tissue is studied extensively in order to determine the properties and causes of permeability changes.[1] Early researchers carried out simple studies on the vertebral endplate. These began with macroscopic sections of tissue subjected to fluid pressure gradients. Sheep endplates exhibit fluid direction, tissue maturity, and regional dependencies.[4] With more complex tissue processing techniques, it is possible to obtain data for IVD tissue.[15] Gu et al. investigated the differences in permeability for different grades of degeneration and age and found that hydraulic permeability values ranged from $1.147*10^{15}$ to $1.924*10^{15}$.[15] The magnitude of this difference is not surprising considering the differences in age and disc grade. Confined compression experiments are able to solve for strain-dependant permeability coefficients, and these values have been seen to change by as much as a factor of 5 for human IVD.[24] As recently as 2007, Henegan and Riches proposed an experimentally determined model for bovine confined compression permeabilities.

$$k(\lambda) = 1.59 * 10^{-15} (\frac{\lambda - 0.2}{0.8})^{1.13} * e^{\frac{-0.02(\lambda^2 - 1)}{2}},$$

Equation 1 - Permeability as a function of stretch ratio

where k is the permeability and λ is the stretch ratio.

Eq. 1 indicates that reference configurations and initial values for tissue testing have a huge impact on derived constants, preloading to even small strains will affect permeability measurements. When swelling is linked to strain, human IVD expansion will be quicker than compression.[36] Alternatively, the permeability through the disc decreases with compressive strain. Permeability of the IVD also changes with applied strain and has a large impact on *in vivo* health of bovine IVD.[17]

Even more advanced experimental setups utilize radiotracer fluids and CT scanning to obtain permeability data, but the resolution of these experiments is somewhat limited and are unable to be resolved within the IVD. Models based on this data incorporate both intrafibrillar and extrafibrillar water contents to build dual porosity simulations.[20] Alternatively, fluorescence recovery after photobleaching (FRAP) techniques have been used to track fluorescein in order to determine the diffusion coefficients for bovine IVD tissue.[42] Research has determined that simple diffusion is sufficient for nutritional supply to the cells of the human non-degenerate IVD, but larger molecule solute transport relies heavily on swelling and loading.[12]

Human IVD AF has been shown to exhibit anisotropic permeability. Table 1 and Figure 3, reproduced from data presented by Gu, demonstrate the high degree of anisotropy present in permeability constants within the AF further reinforcing the concept of inaccurate assumptions about isotropy and homogeneity within the IVD.[15]

Grade/Age years (Min., Max)	Direction	Permeability (10^{-15} m^4/Ns mean ± SD) n=10
1 (13, 27)	Axial	1.530 ± .054
	Circumferential	1.147 ± .056
	Radial	1.924 ± .046
2 (9,49)		
	Axial	1.639 ± .075
	Circumferential	1.559 ± .021
	Radial	1.739 ± .073
3 (50,75)		
	Axial	1.643 ± .113
	Circumferential	1.618 ± .043
	Radial	1.675 ± .095

Table 1 - Hydraulic Permeability Coefficients of Human Lumbar Annulus Fibrosus.[15]

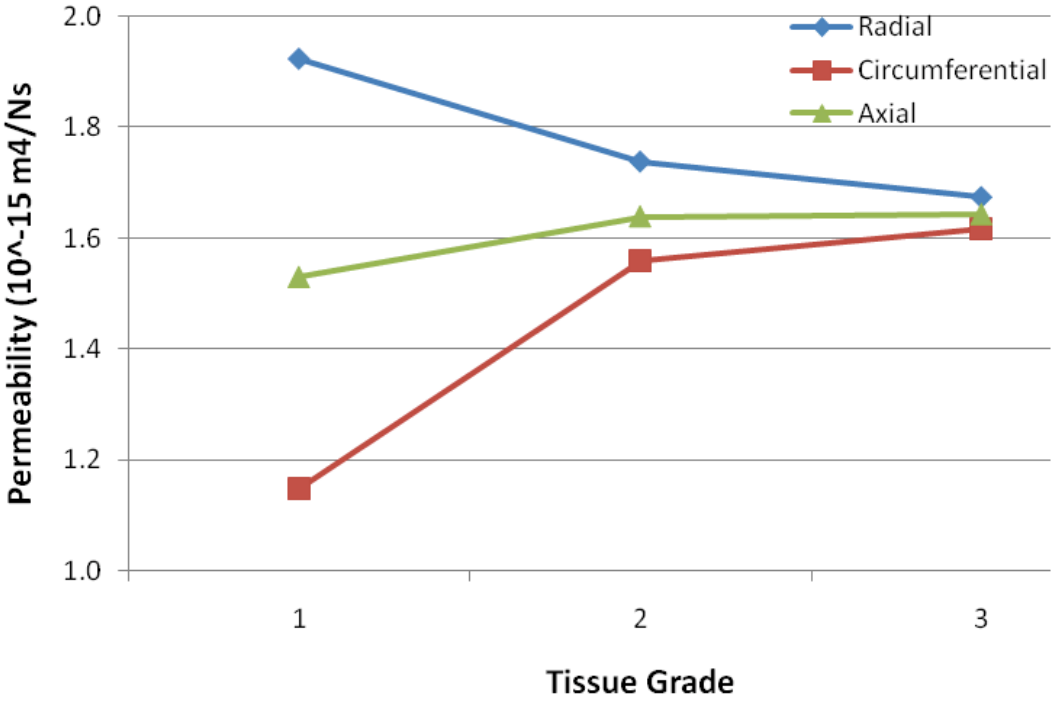

Figure 4 - Graphic representation of Table 1
shows the effect of tissue grade on permeability. This data also highlights the degree of anisotropy in healthy Grade 1 tissue.[15]

Despite the wide range of different methods used to obtain permeability data for the IVD, there is a rough agreement in the resulting experimental values. Authors have examined the effects of age, degeneration, hydration, and loading to name a few. Anisotropy throughout all the tissue is clear and has a large impact on predicted outcomes for anatomical observations on both the macro and micro scales, namely porosity since it has such direct influence on permeability and ultimately tissue properties.

2.6 - Porosity

The effect of porosity is another major topic of discussion and debate within the community. Studies of articular calcified cartilage indicate that porosity may occur on different levels.[7] SEM imaging shows fluid channels of different magnitude which most likely indicate that there is a complex network of channels analogous to a city road system; large highways for heavy traffic and smaller adjacent roads for local traffic. This would explain how cells in the IVD obtain nutrients throughout the whole disc and not only in localized areas near the "highways." Nutritional supply of the IVD is provided primarily by diffusion but also supported by mechanical means through gravity and normal mechanical loading of the spine. Previous studies have demonstrated that diffusive transport of small molecules alone is sufficient for healthy cell function in the IVD, but fluid flow through the disc is necessary for transport of larger molecules.[12] Complex transport kinetics govern nutrient transport and the morphology of the IVD controls the anisotropic and inhomogeneous fluid transport.[42]

Fluid mass transfer within the IVD occurs in all directions. However, investigation into the vertebral endplates adjacent to the IVD in the axial direction show that the highest amount of mass flow occurs above the nucleus pulposus at the center of the disc and decreases radially outward.[4] Furthermore, the flow resistance is approximately 40 times higher outward from the disc than into the disc. Qualitative studies have been carried out

using dyes or small solute transport but quantitative studies are few.[5,20] The cartilage endplate is the limiting factor for fluid transport, as the CE is nearly seven times less permeable than the IVD itself.[4] In one diurnal cycle, the IVD loses as much as 20% volume due to fluid transport.[12]

The study of fluid flow through the disc relies on complex morphological attributes. Furthermore, the disc is not simply an isolated unit that stands alone. The IVD has a strong dependency on the properties of the entire surrounding area (i.e. the vertebral bone and marrow spaces, the AF, and the NP) in order to remain functional and keep the cells within alive. Studying the porosity of the tissues of the IVD will lead to more accurate mathematical descriptions and models. Of great interest is the study of the cartilaginous vertebral endplates since the endplates have such substantial influence in the entire region by serving as the transition point between the soft tissue of the IVD and the mineralized vertebral bone while also allowing for fluid transport to assist with mechanical integrity and strength.

2.7 - Cartilaginous Endplate

The cartilaginous endplate plays an important role in both the mechanical and chemical properties of the IVD segment. The major nutrition pathway of the AF and NP is through the CE. Solute size and shape combined with proteoglycan content of the CE have a direct correlation to the acceleration of proteoglycan loss from the NP which implies that study of IVD degeneration would also require insight into the proteoglycan (or alternatively, permeability) content of the endplate.[37]

The endplate is typically considered to be susceptible to mechanical failure because the CE is considered to be the weak link of the unit. Microscopic observations and autopsy studies show that endplate separation from bone and then the disc is a primary method of failure.[41] Also, FEM simulations indicate that the primary method of failure for the endplate is separation from the subjacent bone.[29] This would indicate that the mechanical properties of

the endplate would be of primary interest in failure studies and that the tissue transition regions need to have further study. The large incidence of Schmorl's nodes (~70% at autopsy of the elderly), which are protrusions of disc tissue into the adjacent vertebra, require careful attention due to the mechanical function and integrity of the CE.[27] A logical study would encompass the histochemical and fluid properties of the CE and their changes with time and/or environment because of the high failure rate and subsequent effects on disc degeneration. The present investigation contains many of the above elements.

After achieving skeletal maturity, the CE remodels, becomes mineralized, and ultimately gets resorbed and replaced by bone. These changes likely inhibit diffusion and likely have large effects on permeability.[28] Morphological changes alter the structure, and these effects will compound with disc degeneration. Scrutiny of the CE is necessary because of the far reaching effects on models and simulations due to porosity being the major contributor to fluid flow of the region and ultimately mechanical properties.

3.0 - Materials and Methods

3.1 - Specimen Preparation

All tissue used in this study was discarded tissue and therefore subject to minimal acquisition and processing protocols. However, all appropriate approval for humane and necessary treatment was followed. Furthermore, all required safety protocols of handling biological tissue were also carefully followed.

For this study, human lumbar spines were obtained from the University of Colorado Health Sciences Center. Tissue was considered discarded due to previous use and processing following previous IRB approved studies in the OrthoBiomechanics Lab at the University of Colorado, Denver (UCD) School of Medicine. The OrthoBiomechanics Lab donated the spines to this study. Vertebral segments (bone-disc-bone) were sectioned with a band saw and the discs subsequently removed while frozen. Tissue was subsequently processed as outlined below.

Rat tissue was also considered to be discarded tissue obtained from an IACUC approved study with the Mahoney group from the Department of Chemical Engineering, University of Colorado, Boulder (UCB). The UCB Veterinarian affirmed no IACUC needed for the present work. Female rats were sacrificed with CO_2 asphyxiation and subsequent cervical dislocation. Lumbar regions were removed, cleaned with a sharp blade to remove all excess muscle and connective tissue, vertebral segments sectioned, and processed within 24h of death.

3.1.1 - SEM Imaging

For a full protocol of SEM sample preparation, see Appendix 1.

Method 1:

Vertebral segments were immersed in room temp 2-methylbutane (2-mb) inside a small metal container. The container was quickly placed into liquid nitrogen until 2-mb crystals formed on the inside surface. The sample was removed and a scalpel was placed in the middle of the disc, or fracture site. The blade was hit with a hammer and the resulting tissue segment placed into Acetone at -85C for one week. The sample was critical point dried with CO_2, mounted with silver colloidal paint onto a SEM stub, coated with ~3 nm Ag, and imaged.

Method 2:

Preparation was the same as Method 1 with exceptions beginning after freeze fracture. Tissue segments were placed into a graded ethanol series, transitioning from 70% ethanol/DI water to 100% ethanol in one week with equivalent intervals at -20C. Samples were critical point dried with CO_2, mounted with silver colloidal paint onto a SEM stub, coated with ~3 nm Ag, and imaged.

Method 3:

Same as the above two methods with the exception of an additional step after fracture and before ethanol or acetone substitution. At this time, the samples were placed into sodium hyperchlorite (regular bleach) and agitated for a period of 5 minutes before going into either acetone or alcohol.

Method 4:

Cut the tissue across the transverse plane of the disc and remove the adjacent vertebra for subsequent ethanol series drying and imaging.

All of the above methods were carried out with care to ethical animal and human tissue regulations. Samples were dissected on cold plates at an approximate temp of -20C in order to maintain the frozen state during dissection.

3.1.2 - Histology

For histology, 11 Sprague-Dawley rat spines were extracted and removed of all unnecessary surrounding tissue; then dried using a graded ethanol series (70-100%) over a 7 day period, cleared with acetone for 24 hours, and embedded in PMMA. (Full protocol in Appendix 3)

The embedded spines were then sectioned transversely across the vertebrae and then again across the spinous process using a diamond saw wafering blade, polished with a graded series of silicon carbide paper from 300-1200 grit, and further polished with 9, 3, and .5 μm diamond paste. The spines were stained with Toluidine blue according to a protocol set out by Ayers et al.[6] (Full protocol in Appendix 4) or Massons' Trichrome. Stained sections were imaged with a bright field microscope.

3.2 - Image Analysis

Image analysis was carried out using ImageJ software.[34] SEM images were first adjusted with brightness and contrast to the half maximum of the Gaussian distribution of the image color on the dark side of the curve and were then thresholded for intensity and subsequently analyzed for area fraction. Pore sizes were compared to those found with histological methods.

Histological images were overlaid to form composites of whole IVD segments. Toluidine Blue and Massons' Trichrome staining enhanced anatomical features and helped to differentiate calcified regions from undecalcified regions. Cartilaginous endplates were

broken into 5 equal "Zones" based on the overall length (proximal to distal of the spinal cord), each of equal length.

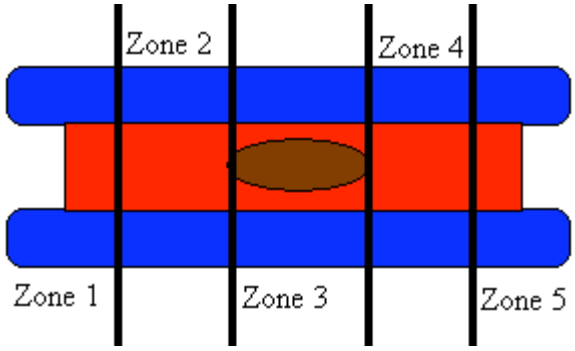

Figure 5 - Zone Designations
shows the breakdown of inspected 'zone' locations. Zones were based on isolation of anatomically similar regions of the IVD..

3.3 - Analytical Approach

The porosity constants presented in literature are derived from one of two ways: back solved for from permeability data or based on fractional water content. Both of these methods assume a fully homogenous and isotropic system with an even distribution of pores of all of the same size; however, the IVD is neither homogenous nor isotropic. Therefore, direct measurements of porosity are made in order to supplement and improve existing data. Even more disconcerting is the fact that existing data supports the concept of anisotropic permeability. A thorough search of the literature show no publications that conducted measurements to obtain these constants *in vivo, ex vivo,* or *ex vitro*.

Darcy's Law is a constitutive equation derived from water flow through sand, and describes fluid flow through a porous medium.

$$Q = \frac{-k}{\mu} A\left(\frac{P_B - P_A}{L}\right)$$

Equation 2 - Darcy's Law

The total discharge, Q (units of volume per time, e.g., m^3/s) is equal to the product of the permeability (κ units of area, e.g. m^2) of the medium, the cross-sectional area (A) to flow,

and the pressure drop ($Pb - Pa$), all divided by the dynamic viscosity μ (in SI units e.g. kg/(m·s) or Pa·s), and the length L the pressure drop is taking place over. The negative sign is needed because fluids flow from high pressure to low pressure. So if the change in pressure is negative (in the x-direction) then the flow will be positive (in the x-direction).

Furthermore, dividing Q by the area A nets the flux q (flow/unit area). This, combined with the porosity yields the velocity of the fluid through the medium.

$$v = \frac{q}{\phi}$$

Equation 3 - Fluid Velocity through a Porous Medium

and

$$\phi = \frac{V_w}{V_T}$$

Equation 4 - Fluid Fraction of Porous Medium

where V_W is the volume of water (or fluid) and V_T is the total volume. With relation to IVD observations made in this study, V_W is the volume fraction of observed pores and V_T is the total area measurement.

IVD measurements focus on obtaining the permeability constant k, and modified to these measurements the following form of Darcy's Law is used.

$$k = \frac{Q}{\Delta P} * \frac{h}{A}$$

Equation 5- Modified Darcy's law

k is the permeability coefficient k, defined by this equation with dimension $m^4/N*s$, A is the permeation area of the sample, and h is the thickness of the sample. The only change in Eq. 5 from Eq. 2 is the loss of μ which translates to k being of different dimensions. Eq. 5 is the commonly used form of Darcy's Law when applied to IVD tissue.

A new empirical model has been presented by Gu based on his experimental data that

describes the permeability of agarose gels and cartilage more accurately than was previously unable to be achieved with any mathematical models.[16]

$$k = a * \left(\frac{\phi_W}{\phi_S} \right)^n$$

Equation 6 - Experimental Permeability

In this case, a and n are constants that depend on the structure and composition of the media. For cartilage and agarose gels, the values for a and n are .00339 nm^2 and 3.236 respectively. Since porosity changes with deformation, this model can also describe strain dependant permeability due to the change of $\left(\frac{\phi_W}{\phi_S} \right)$.

4.0 - Results

SEM imaging provided a large range of quality results due to the various experimental protocols. These results further reinforce the inherent variability and difficulty with soft tissue SEM. While all of the methods should produce accurate results, all were investigated in order to confirm which method minimized the amount of sample loss due to delamination, off plane cuts, too fast or too slow dehydration, and exposed surface defects. Processing surface damage, lamellar tear failure, indistinct bordering between architecture, and stress relief due to cutting were all observed effects surface damage due various processing methodology.

The primary source of results obtained for this thesis for SEM images was through the blade cutting, graded ethanol series, and critical point drying. Porosity and CE thickness results were obtained through PMMA embedding and histological staining. Experimental results were compiled into summary plots and charts for further analysis. Appendix 2 shows alternative method preparation results.

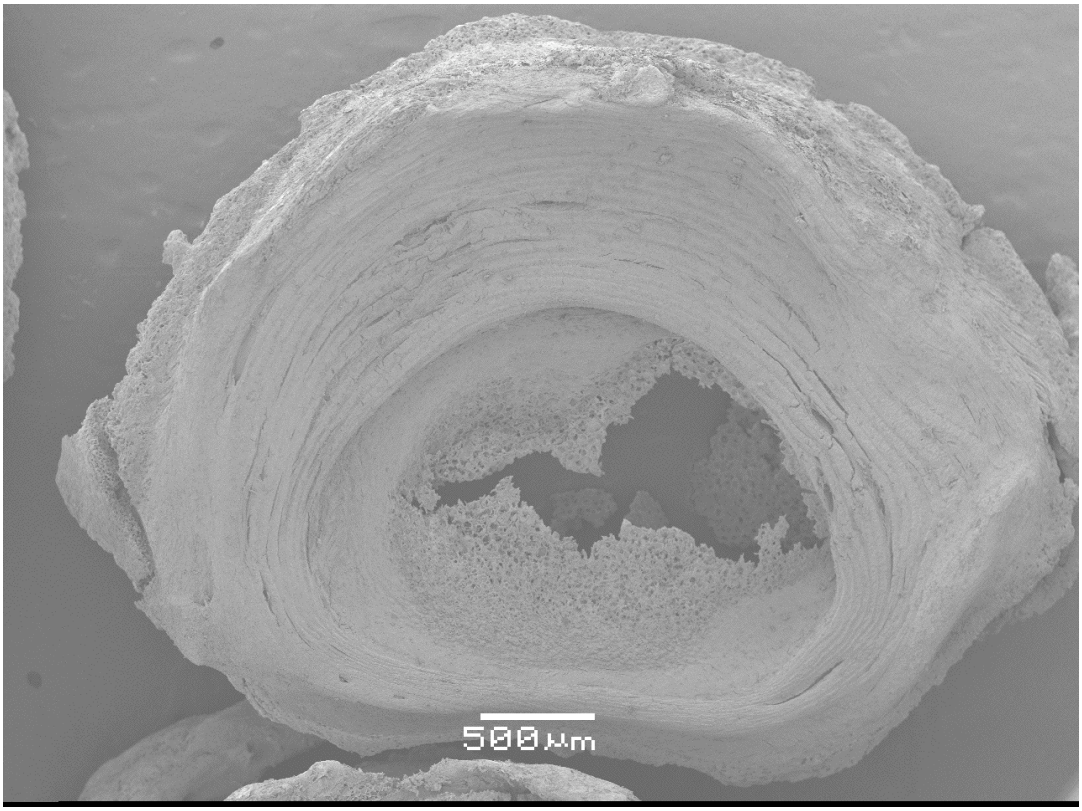

Figure 6 – Whole IVD Cut Bleach EtOH
preparation showing SEM of two different regions of interest in the rat tail intervertebral disc: nucleus pulposus demonstrating: (a) fine collagenous structure of the rat nucleus pulposus; (b) cellular inclusion from nucleus pulposus cells demonstrating area where cell was present; and (c) high-magnification image of cellular inclusion demonstrating fine structure of pericellular matrix.

Figures 6-12 are a zoom series of the highest quality sample showing porosity at different scales. Figure 6 was prepared by cutting in the axial plane across the IVD midway between adjacent vertebrae. The sample was then immersed in bleach for 1 min with agitation and subsequently immersed in a graded series of ethanol (70%-100%) within one week. The sample was then critically point dried with CO_2, coated with ~5nm of Ag, and mounted on an aluminum stub using colloidal silver paint for SEM imaging. While this preparation method resulted in visible delamination of annuluar layers, Figure 5 shows that the lamellae of the AF are clearly visible. General dimensions and features are shown. Drying artifacts within the AF are manifested as cracks and the significant water content of the NP causes extensive

damage due to drying is also shown. Despite the damage, a clear difference in number and size of pores/porosity between AF and NP can be seen even at this scale.

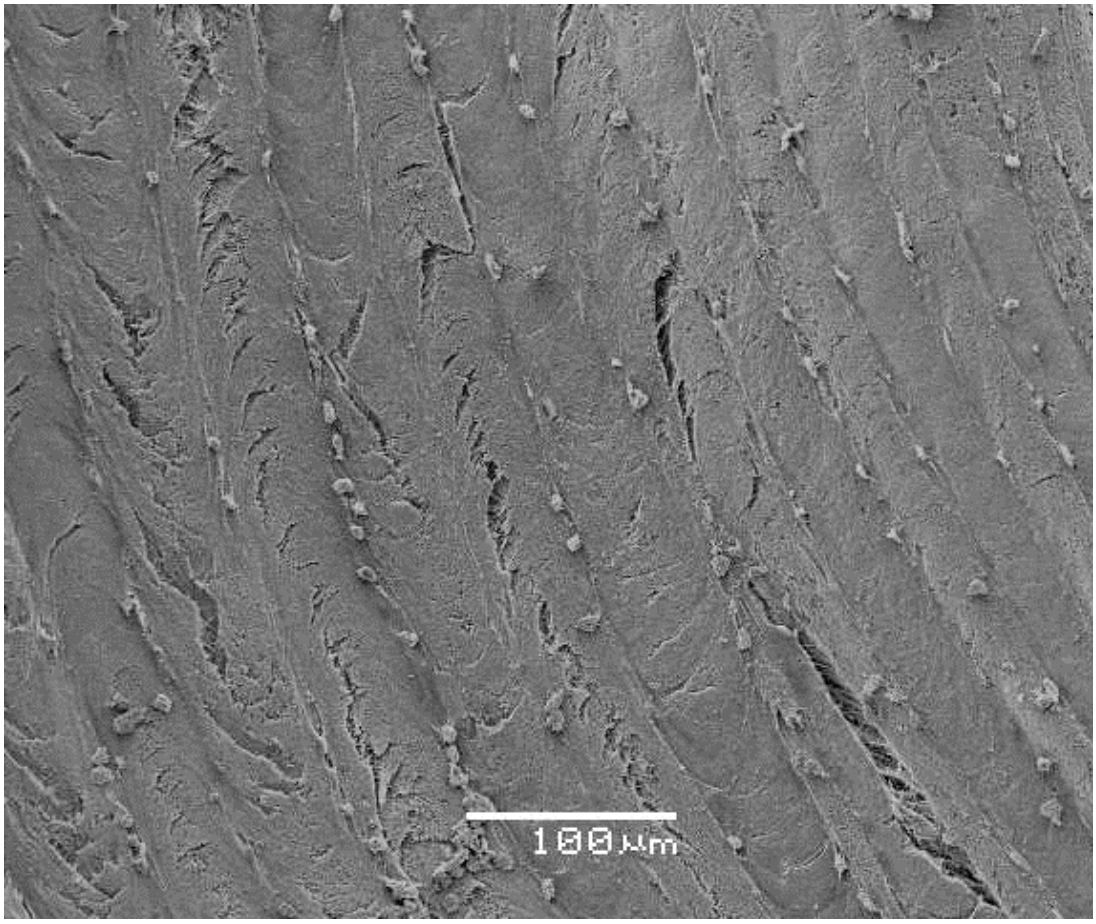

Figure 7 – Lamellae SEM Cut Bleach EtOH
showing the layered structure of the rat IVD lamellae. The different textures indicate the different collagenous orientations within layers and the separation due to dehydration also becomes evident at this scale.

In a single sample, cracking due to drying can be seen at multiple scales (Figures 6 and 7) Large scale cracking is manifested in Figure 7 as channel cracking, and small scale cracking is manifested as notches. Smaller scale porosity is shown at this level as compared to Figure 6 due to the greater magnification. However, very fine pores and fibers are visible but still indistinct. The lamellae are clearly visible and the small 'islands' between lamellae are just visible. The thickness of layers is also visible in Figure 7, and change as a function of radius.

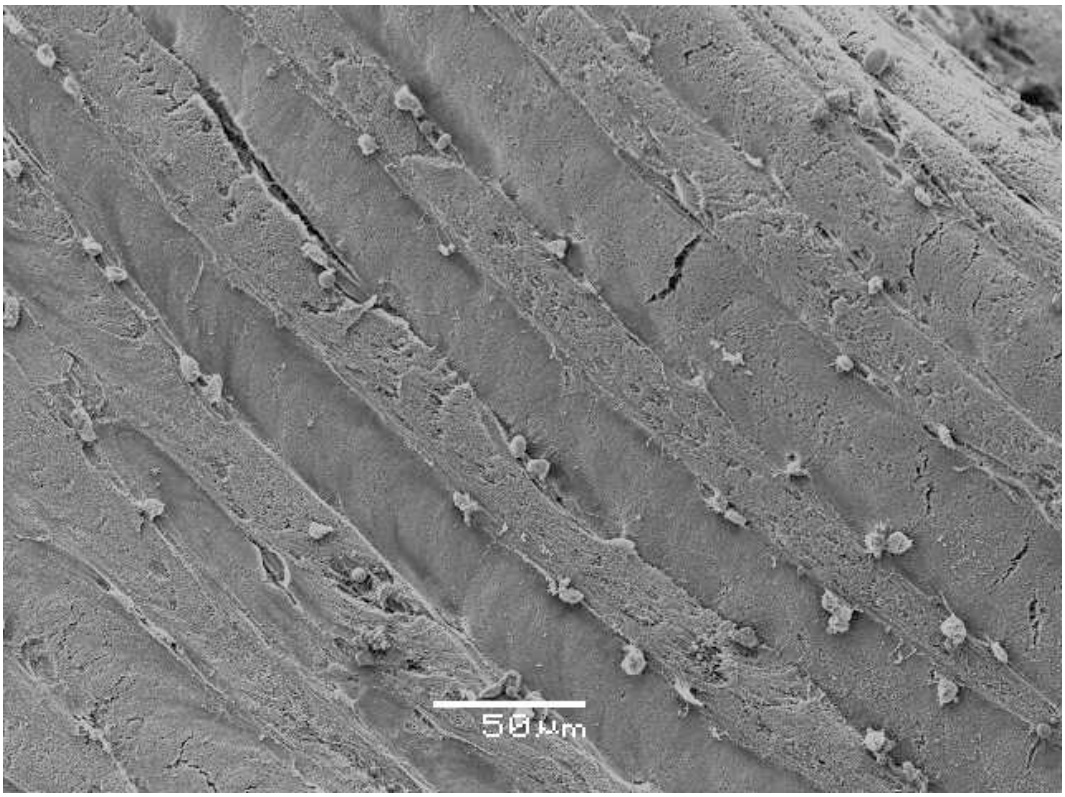

Figure 8 – Layered SEM Cut Bleach EtOH
shows the scale at which pores begin to become visible. Delamination and some minor cracking due to dehydration is evident. The alternating collagen angles between layers is manifested as textural differences.

The same sample preparation method of blade cutting, bleaching, and graded alcohol series was used for both Figures 6 and 8. Figure 8 shows a clearer distinction between lamellae which highlights the alternating fiber orientations between lamellae as the textural differences between layers. Cracking due to drying is still evident, but small-scale porosity is becoming clearer in view. The low relative electron content of soft organic tissue makes it considerably prone to charging, so some areas of Figure 8 have a bleached appearance.

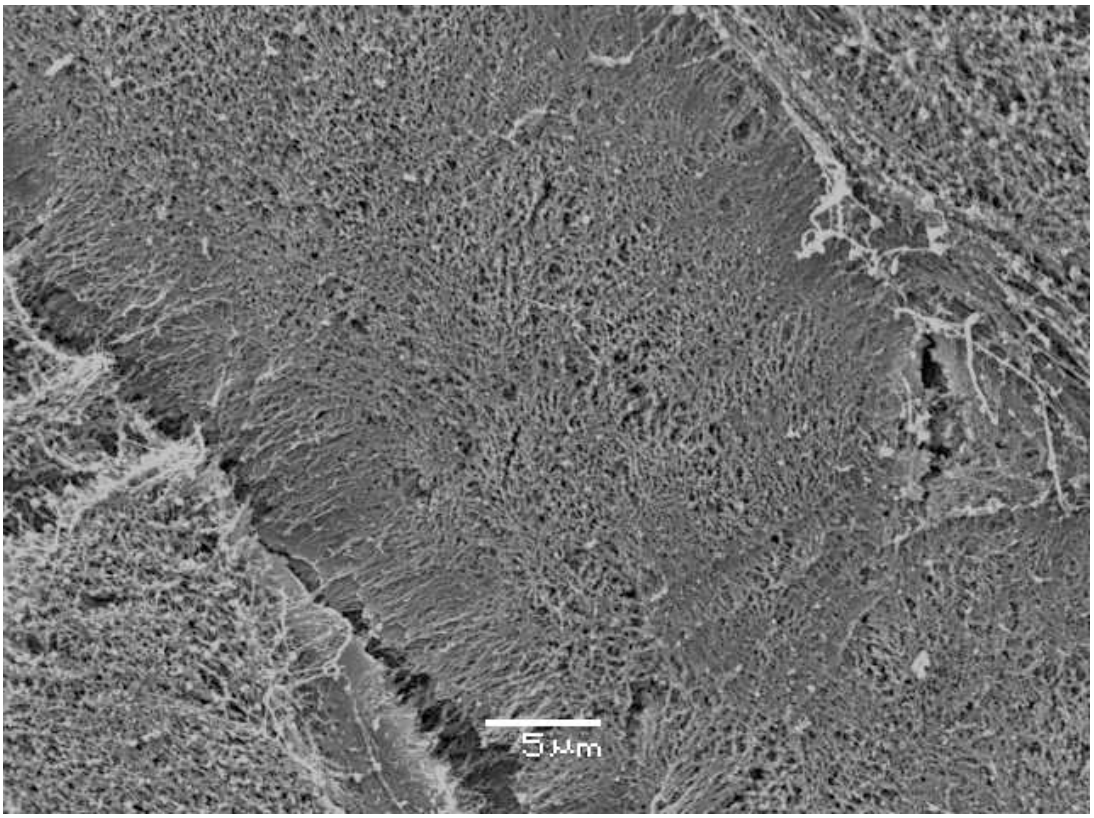

Figure 9 – Single Layer SEM Cut Bleach EtOH
shows the porosity within a single lamellae layer. Fibers connecting between layers is becoming clear, and large scale dehydration effects is minimized. The hierarchical structure of collagen fibers that make up the AF can also be seen.

Figure 9 is the same sample as Figure 6. Cracking due to drying is becoming minimal and the porosity between fibers is quite apparent. Fibers connecting different lamellae are also visible, and the general direction of fibers within lamellae shows alternating between adjacent lamellae. Fibers appear to attach themselves to the locations of greatest mechanical advantage, with general trends following typical paths.

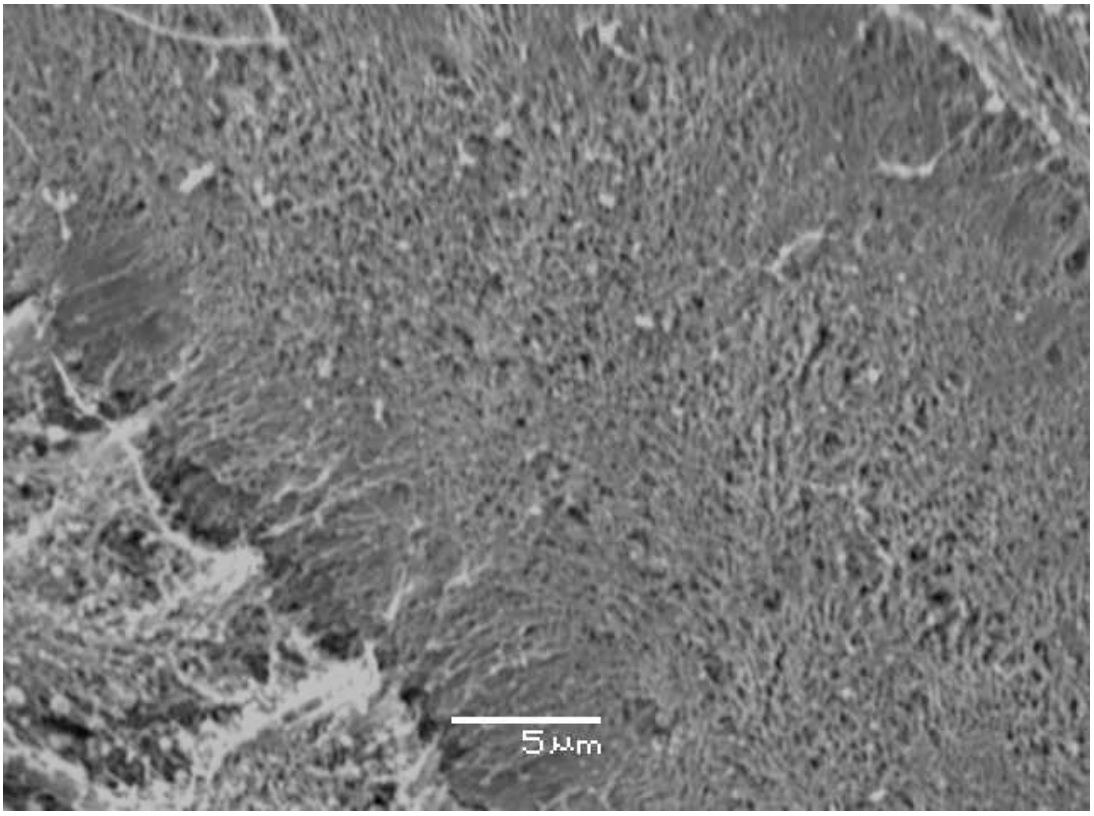

Figure 10 – Single Layer SEM Cut Bleach EtOH
shows the porosity within a single lamellae layer. Fibers connecting between layers is becoming clear, and large scale dehydration effects is minimized. The hierarchical structure of collagen fibers that make up the AF can also be seen.

Figure 10 is the same sample as Figure 6 and serves as an additional data point for porosity calculation confidence by showing distinct borders between visible pores. It also highlights the attachment fibers between layers and clearly shows the fiber orientations within a single layer.

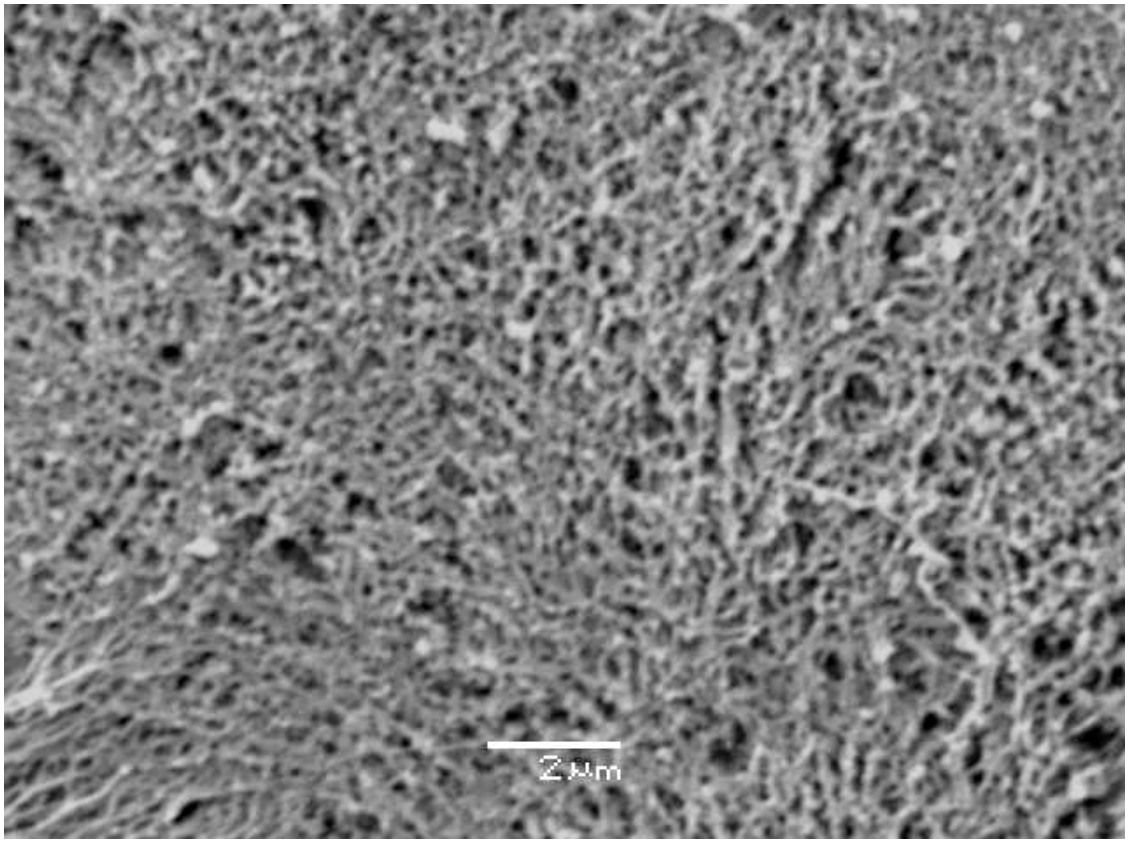

Figure 11 – Close Up SEM Cut Bleach EtOH
shows the visible porosity of the rat IVD lamellae tissue. At this scale, the pore fraction is realized as a much larger portion than at lesser magnifications and implies that the AF tissue is mainly comprised of a very fine fibrous network.

Figure 11 is the same sample as Figure 6, both prepared using blade cutting, bleaching, and the ethanol drying process. Figure 11 is similar to Figures 9 and 10 by clearly showing pore borders. Figure 11 also has the distinct advantage over Figures 9 and 10 with the exclusion of the lamellae border. The exclusion allows for a very accurate measurement of the visible pore fraction at this scale. As a result, the porosity between fibers can be calculated with confidence.

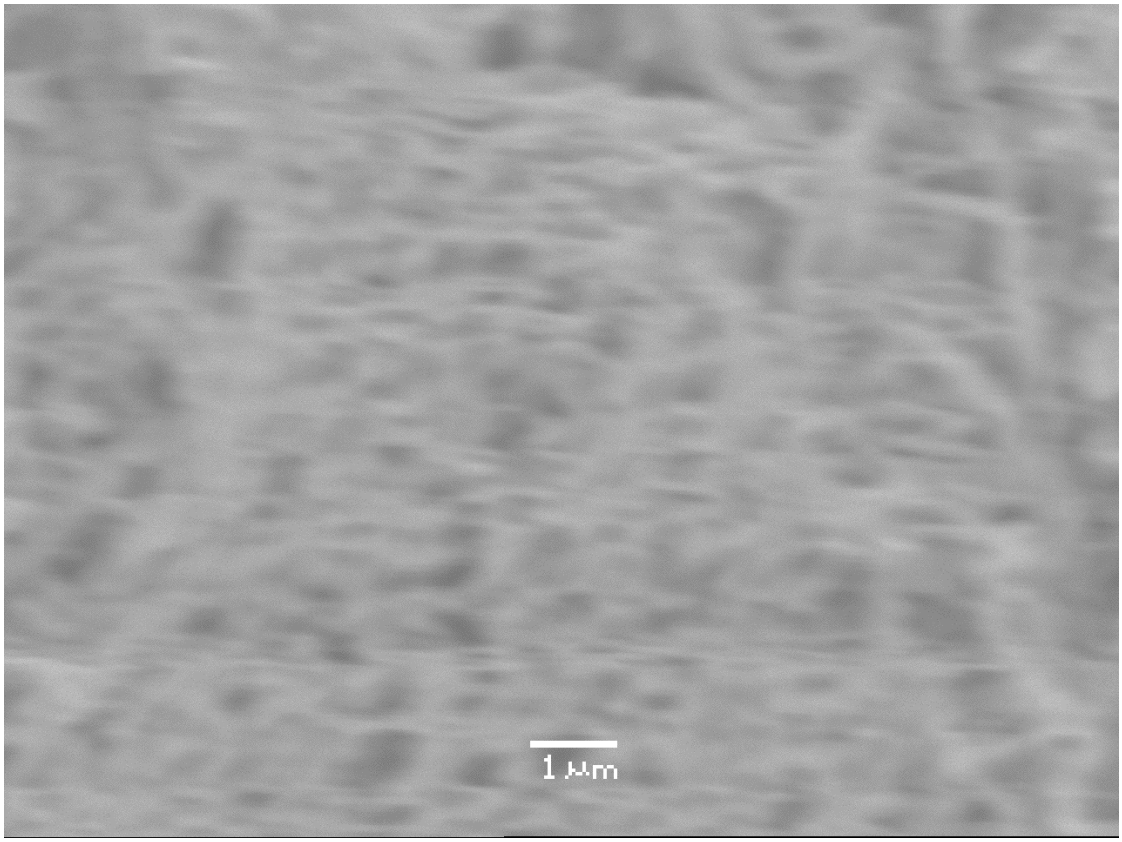

Figure 12 – High Magnification SEM Cut Bleach EtOH
shows the magnification limit of all of the processing methods used in this thesis. The blurred borders indistinct fibers indicate that this image is insufficient for analysis.

Figure 12 serves primarily to highlight the resolution limit of SEM imaging using the JEOL SEM. This tissue and was prepared with blade cutting, bleaching, and graded ethanol series. Since the fibers and pores are blurred and are consequently not useful for analysis.

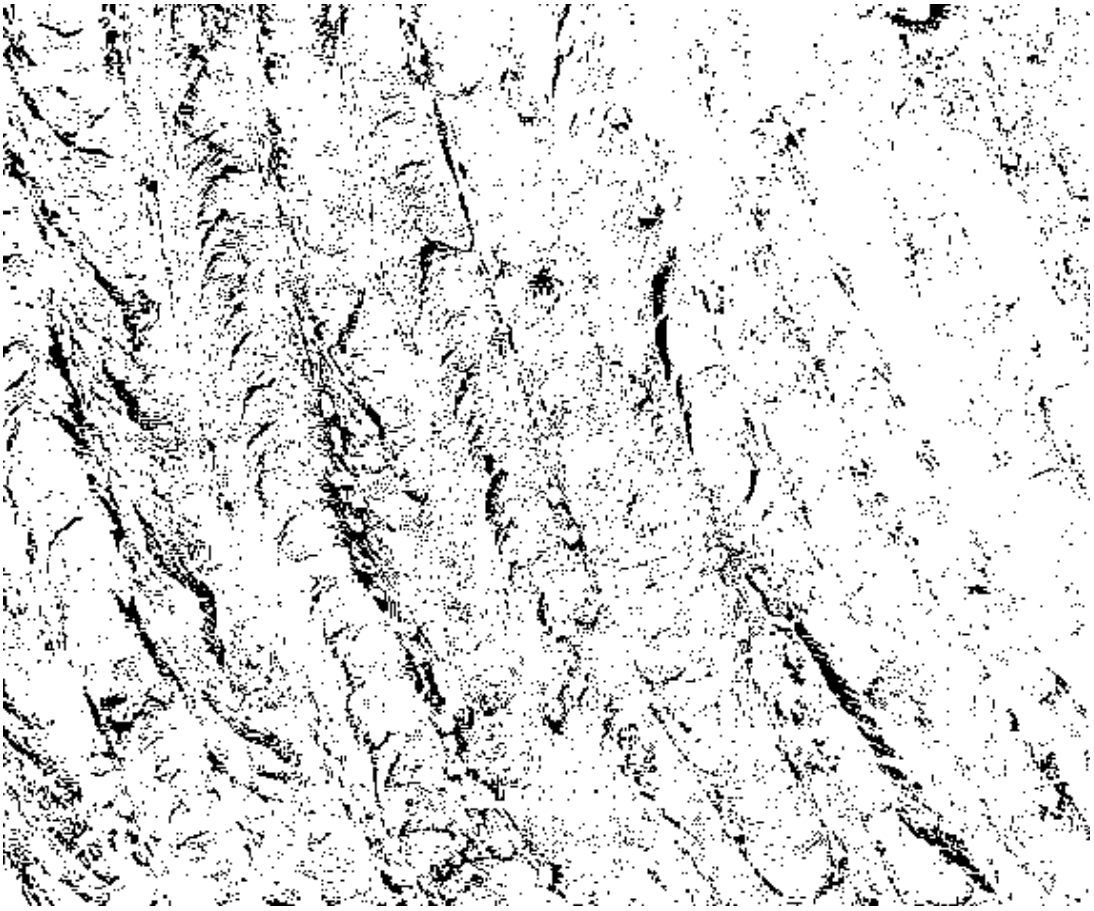

Figure 13 - Porosity Image of Fig 7
shows the mathematical porosity estimation of the sample in Figure 7. This sample was prepared using blade cutting, bleaching, and graded ethanol series. The grayscale for Figure 7 was thresholded based on visible pores and converted to black and white for pore fraction calculations.

Figure 13 is the mathematical estimation of porosity for Figure 7. An estimated grayscale equivalent was chosen for pores and the Figure was thresholded and converted to black and white as shown. The result shows an estimation of the porosity at this scale. Figure 13 yielded a visible area fraction of pores to be 11.5%.

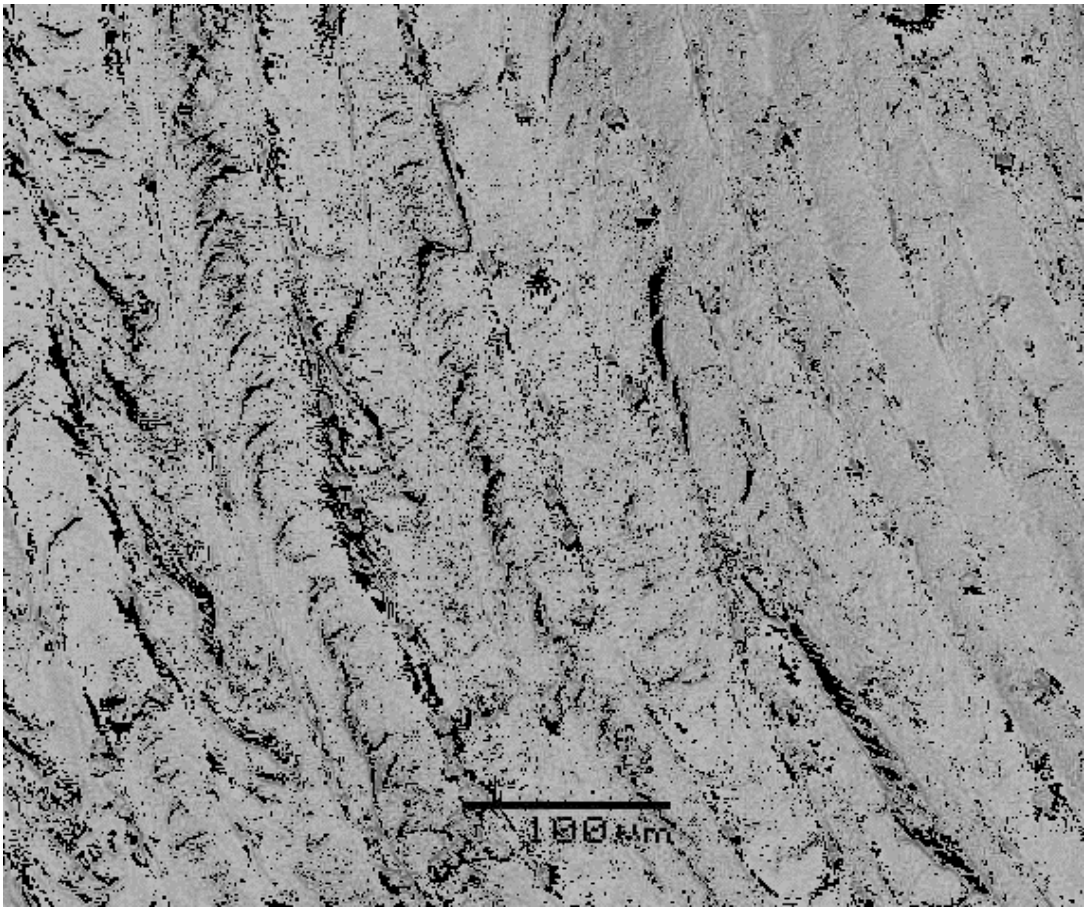

Figure 14 - Image addition of Figs 7 and 13
shows the accuracy of the mathematical estimation of pores. Images 7 and 13 were mathematically added together to produce Figure 14. Figure 14 confirms the porosity estimation to be sufficient due to the remaining contrast areas being visually compatible with the original.

Figures 14, 16, and 18 are for comparison to the originals and are image additions of the original and porosity images. The figures are to confirm accurate image processing and porosity measurements and do so by showing compatibility between the original and processed images.

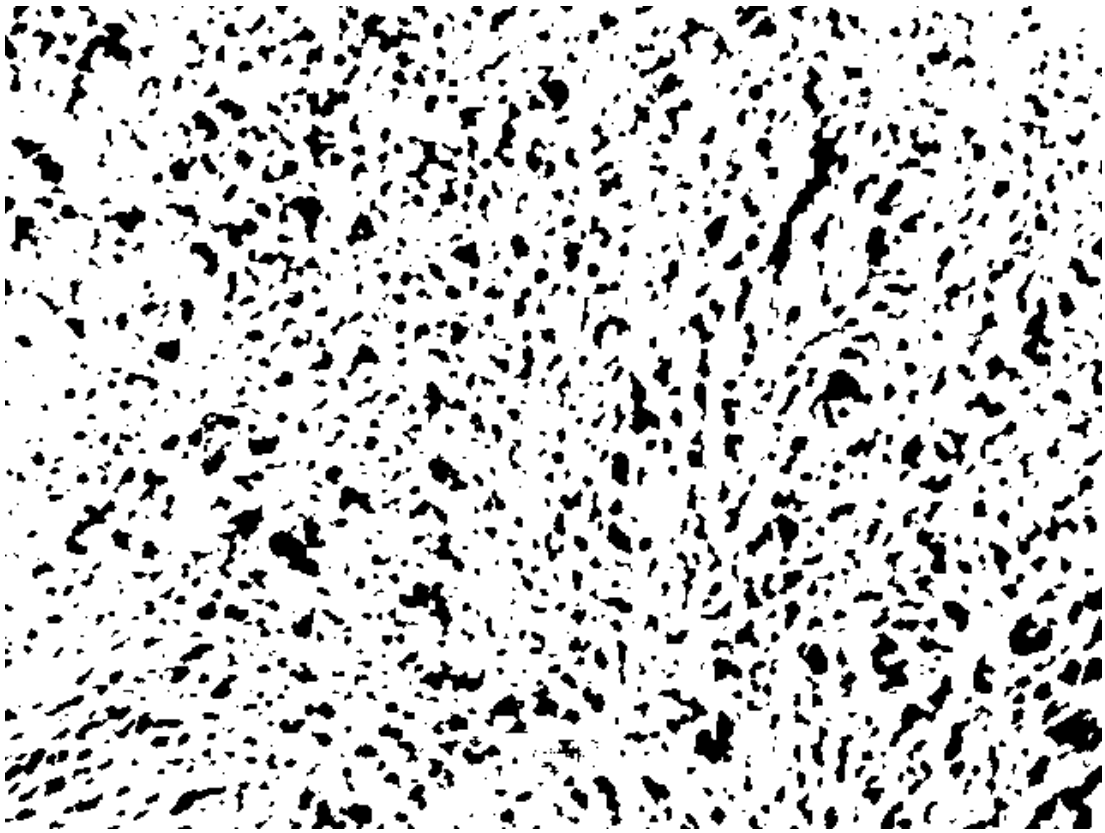

Figure 15 - Porosity Image of Fig 11
shows the mathematical porosity estimation of the sample in Figure 11 which was prepared using blade cutting, bleaching, and graded ethanol series. The grayscale for Figure 7 was thresholded based on visible pores and converted to black and white for pore fraction calculations.

Figure 15 is the mathematical estimation of porosity for Figure 11. An estimated grayscale equivalent was chosen for pores and the Figure was thresholded and converted to black and white as shown. Figure 15 yielded a visible porosity area fraction of 19.06%.

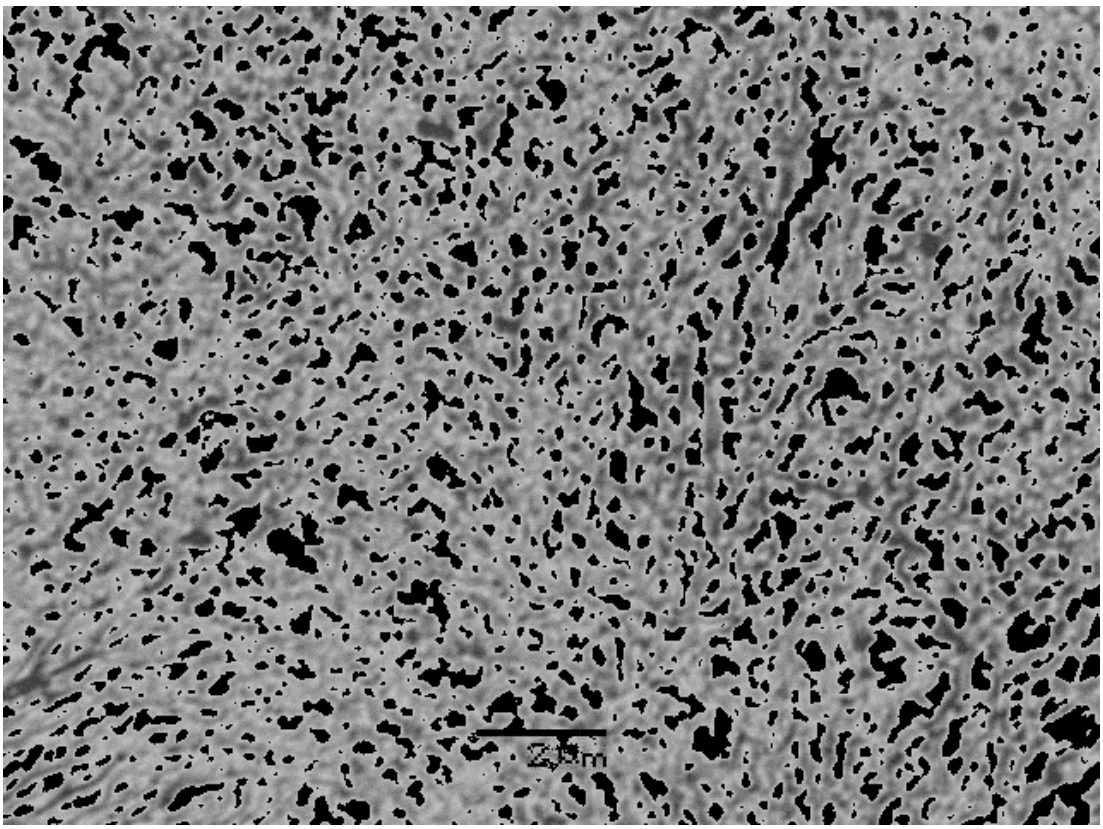

Figure 16 - Image addition of Figures 11 and 15
shows the accuracy of the mathematical estimation of pores. Images 11 and 15 were mathematically added together to produce Figure 16. Figure 16 confirms the porosity estimation to be sufficient due to the remaining contrast areas being visually compatible with the original.

Figure 16 is similar to Figure 14 and provides an additional data point for analysis. The figures are to confirm accurate image processing and porosity measurements and do so by showing compatibility between the original and processed images.

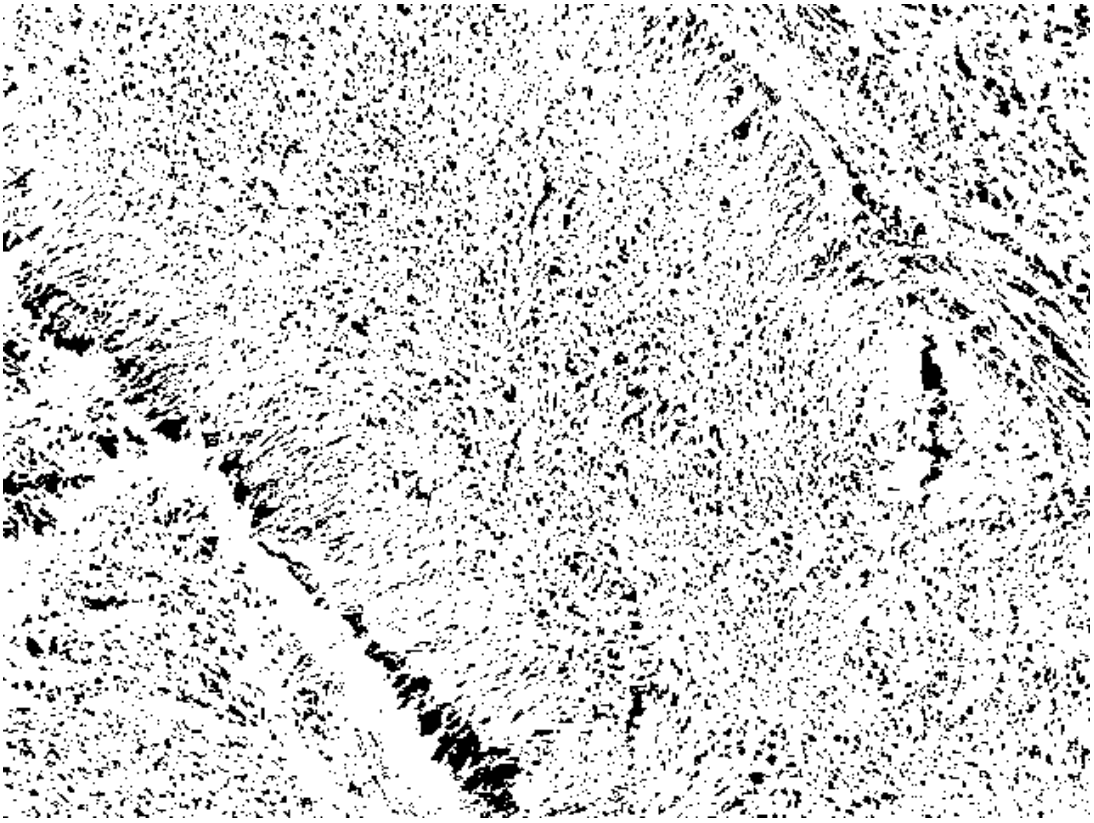

Figure 17 - Porosity Image of Figure 9
shows the mathematical porosity estimation of the sample in Figure 9 which was prepared using blade cutting, bleaching, and graded ethanol series. The grayscale for Figure 9 was thresholded based on visible pores and converted to black and white for pore fraction calculations.

Figure 17 is the mathematical estimation of porosity for Figure 9. An estimated grayscale equivalent was chosen for pores and the Figure was thresholded and converted to black and white as shown. Figure 17 yielded a porosity area fraction of 15.19%.

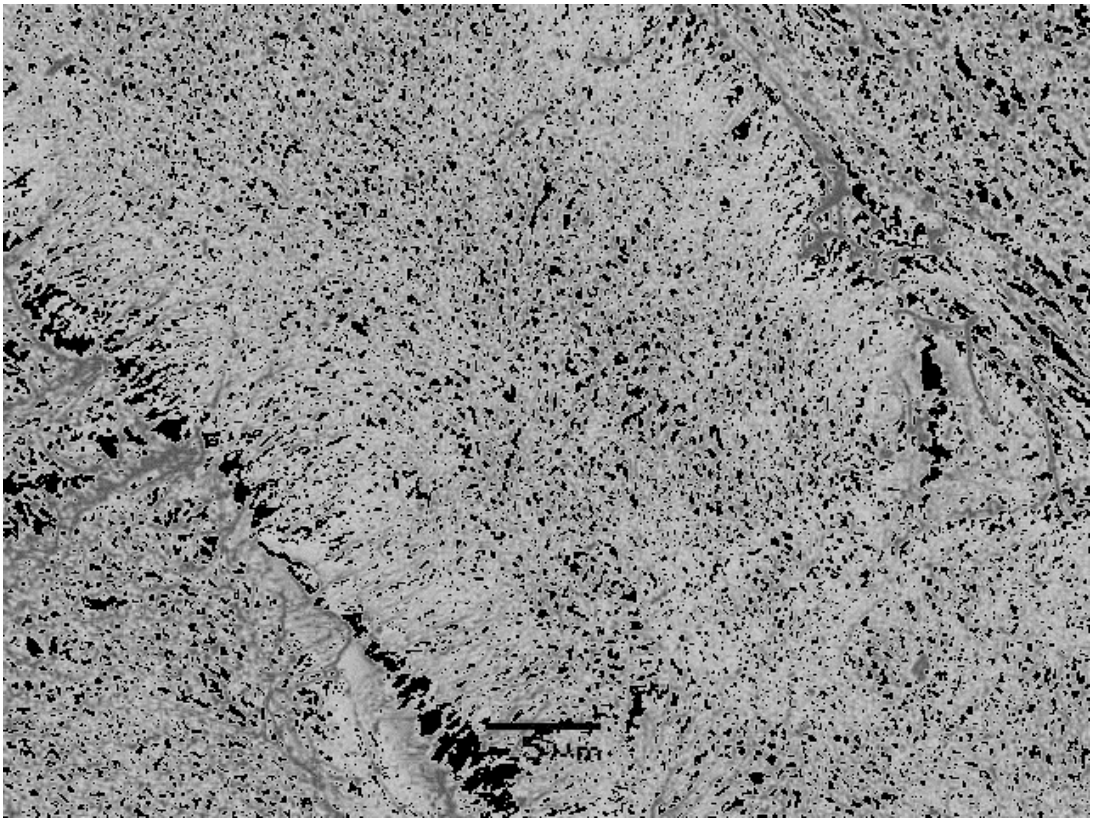

Figure 18 - Image addition of Figs 9 and 17
shows the accuracy of the mathematical estimation of pores. Images 9 and 17 were mathematically added together to produce Figure 18. Figure 18 confirms the porosity estimation to be sufficient due to the remaining contrast areas being visually compatible with the original.

Figure 18 is similar to Figure 14 and provides an additional data point for analysis. The figures are to confirm accurate image processing and porosity measurements and do so by showing compatibility between the original and processed images.

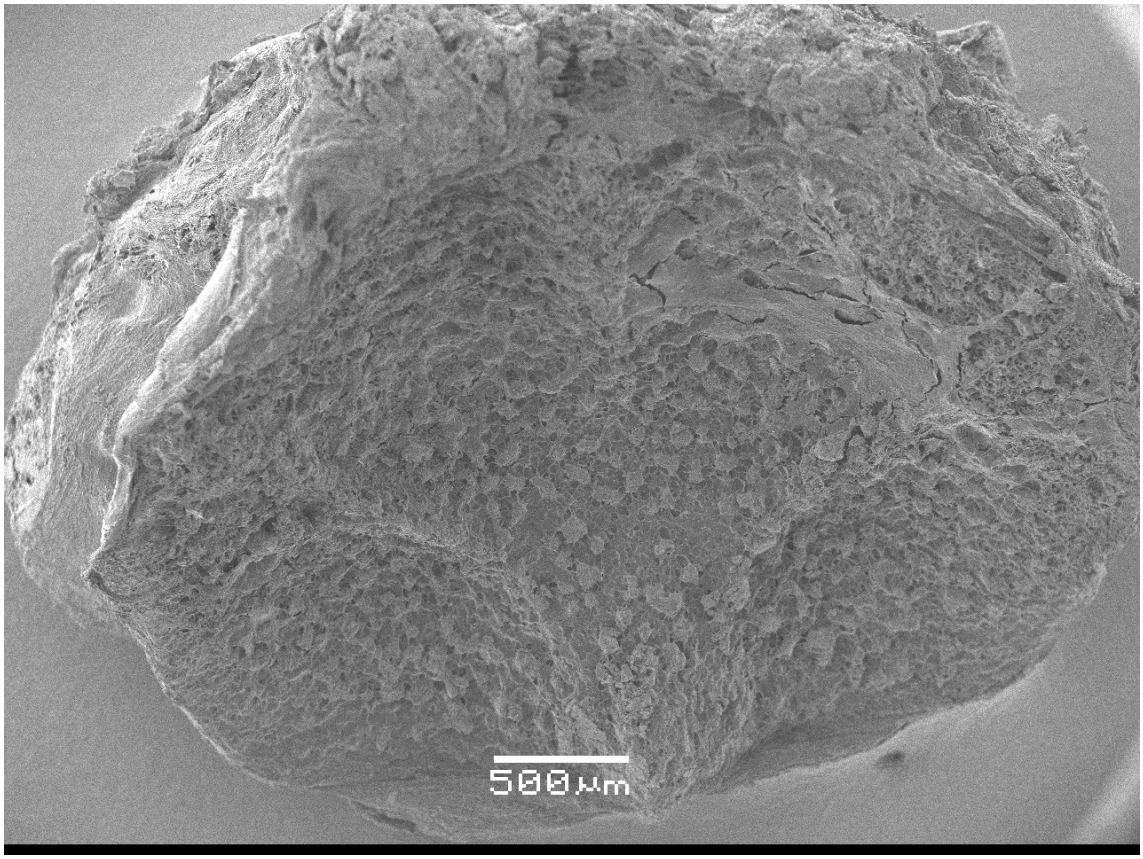

Figure 19 - Full CE Morphology
shows the morphological surface structure of the CE. The sample in Figure 19 was prepared by manually pulling the disc free from the adjacent bone, immersing in acetone at -80°C for one week, and critically point dried. The surface shows features that may play a role in mechanically anchoring the IVD/CE to the adjacent bone.

The samples for Figures 19-21 were prepared by manually pulling apart two adjacent vertebrae, immersing in acetone at -80°C for one week to mitigate accelerated water diffusion effects, and critically point dried with CO_2. The IVD typically remained attached to the cranial vertebrae and the disc was then removed from the remaining vertebrae and the "pulled" surface was imaged. The samples were dried, coated with ~5nm Ag, and attached to an aluminum stub with colloidal silver paint for SEM imaging. Figures 19-21 are SEM endplate images that show raised 'islands' distributed throughout the surface.

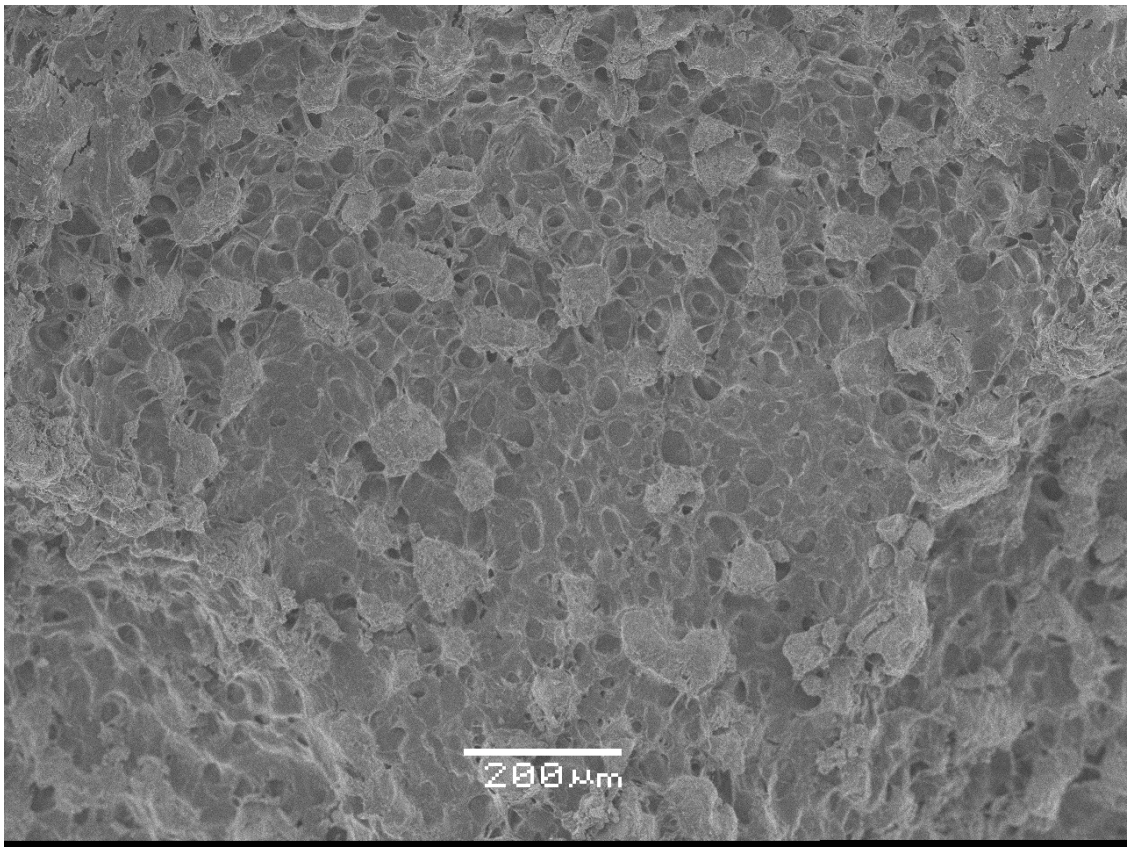

Figure 20 – CE Surface Morphology
shows the morphological surface structure of the CE. The sample in Figure 20 was prepared by manually pulling the disc free from the adjacent bone, immersing in acetone at -80°C for one week, and critically point dried. The surface shows 'island-like' features that may play a role in mechanically anchoring the IVD/CE to the adjacent bone.

Figure 20 shows the raised 'islands' at a higher magnification with approximate diameters ranging from 25 micrometers to 150 micrometers. The 'islands' have a somewhat regular surface and size distribution. Imaging at this scale begins to show the pore structure that permeates from the bone through the CE to the subjacent IVD.

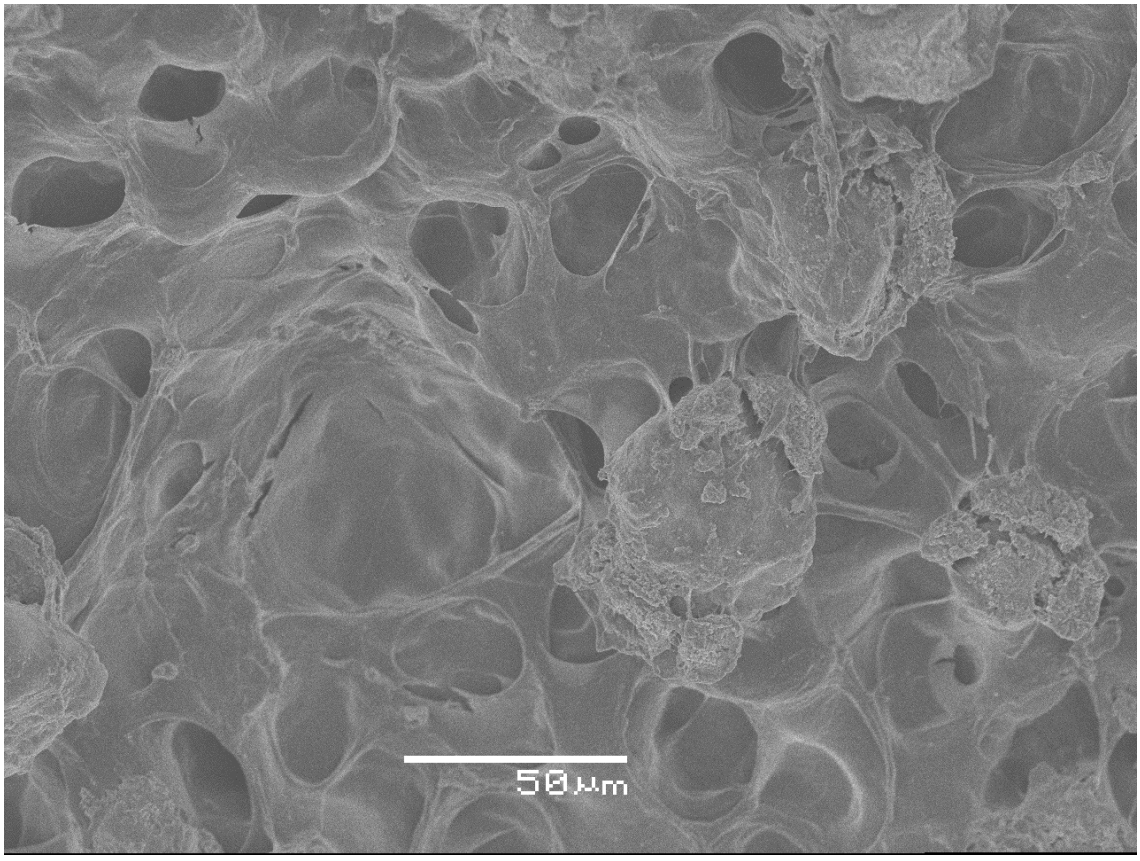

Figure 21 – Morphological CE 'Island'

Figure 21 shows single CE 'islands'. Imaging at this scale shows the 'island' features to be lacking a clearly defined fiber organization. However, the surface appears to have a sponge-like appearance that may contribute mechanically to the properties of the tissue.

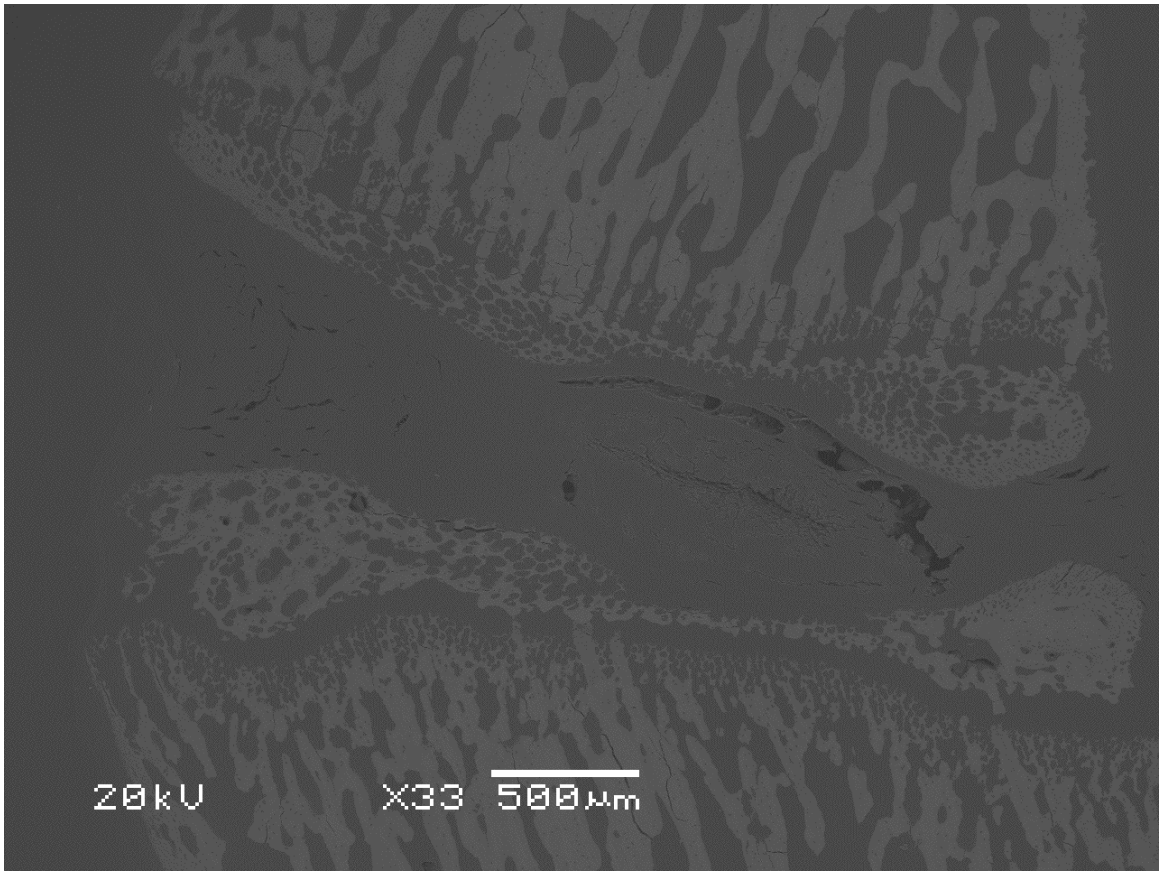

Figure 22 - Backscattered imaging of PMMA embedded vertebral segment shows the vertebrae on the top and bottom with the CE in between. The IVD is difficult to resolve with this method due to its low relative electron content.

BSE imaging of SEM samples helps to show contrast between calcified regions. The sample for Figure 22 was prepared by isolating a single vertebral body unit, embedding in PMMA, sectioning and polishing along the mid-sagittal plane of the unit, coating with ~5nm Ag, and imaging. The soft tissue of the IVD is difficult to view due to the low level of calcification while the CE and bone are easy to view. The raised 'islands' in Figures19-21 are apparent here as fingers linking the CE to the bone which illustrates the possibility of an attachment mechanism between the two anatomical structures.

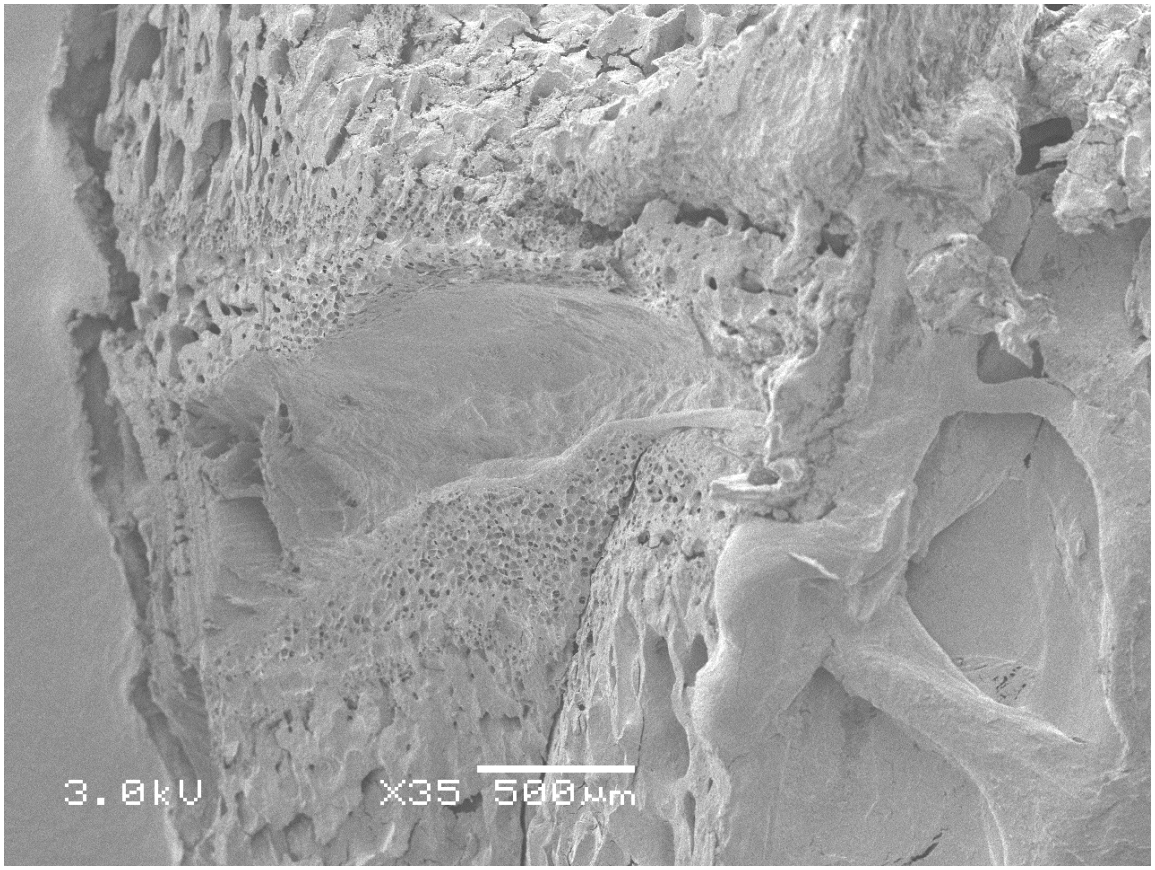

Figure 23 - IVD with CE and Vertebrae on Top and Bottom
showing the pore structure and defined borders between anatomical features.

The samples for Figures 23-25 were prepared by freeze fracture across vertebrae and then sagittally through the IVD, immersion in acetone at -80^{o}C for one week, critically point dried with CO_2, coated with ~5nm Ag, and imaged in SE mode. The cartilaginous endplate is shown in Figures 23-25 and is used primarily to correlate histological results to SEM results to confirm anatomical features. The angled view shows depth and allows for viewing of a few lamellae layers on the far side.

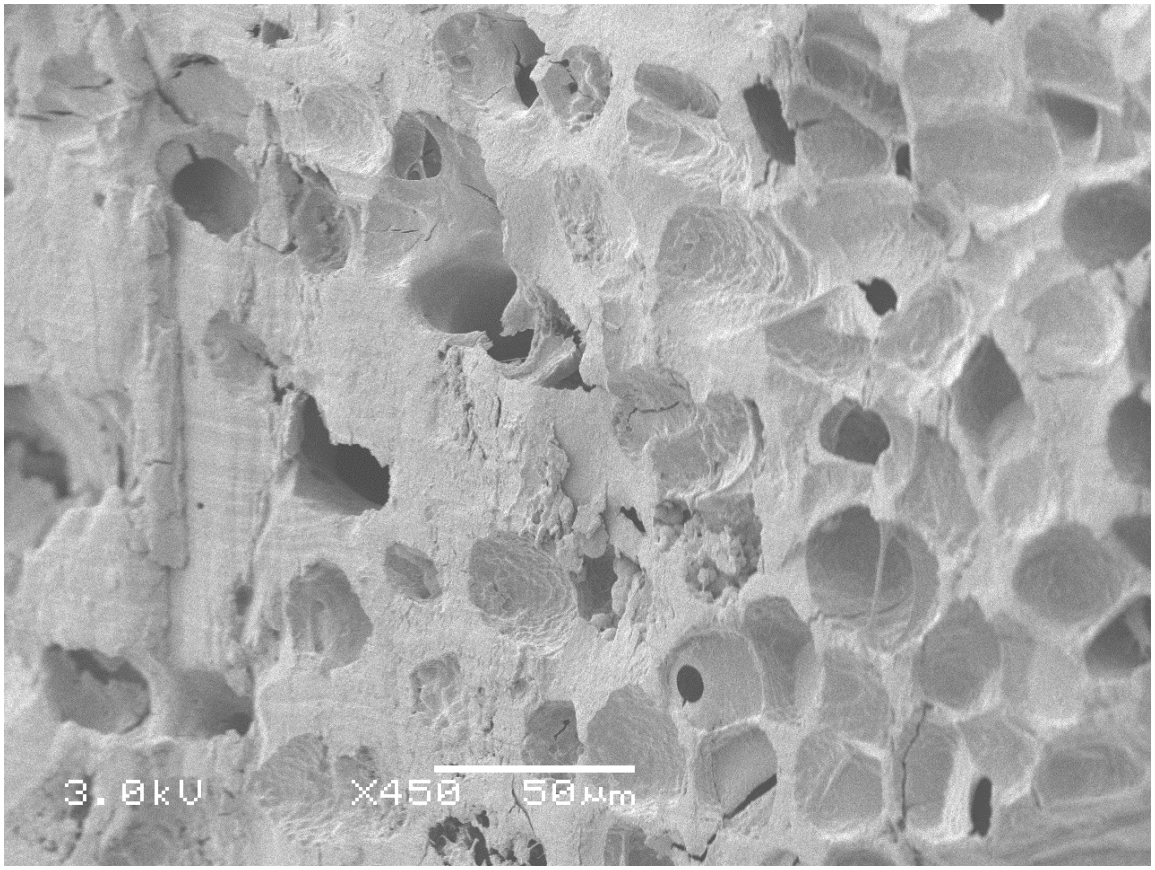

Figure 24 - Cartilaginous endplate of the IVD
showing the porous nature of the structure. Minimal drying effects are observed and results in a uniform distribution of pores throughout.

Figure 24 shows the CE pores with minimal cracking due to drying damage. The pores in this image are an approximate confirmation of histological results.

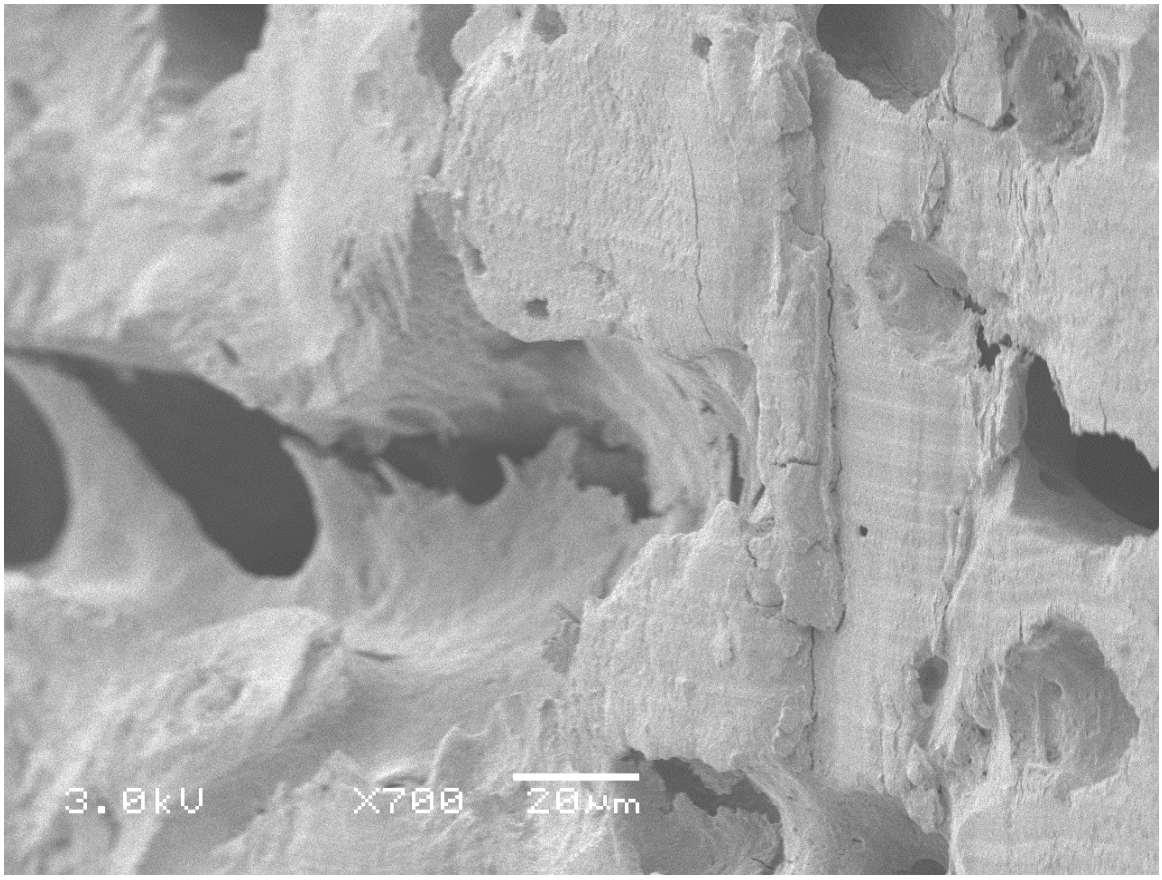

Figure 25 - Cartilaginous endplate of the IVD
showing single pores. The depth of pores is apparent despite minimal damage to the sample manifested as vertical cracking.

Figure 25 shows primarily the quality of the fractured surface. The pores of the CE are still visible and confirm the irregular shape of histological results. Figures 23-25 suggest pore diameters ranging from ~5-30 microns.

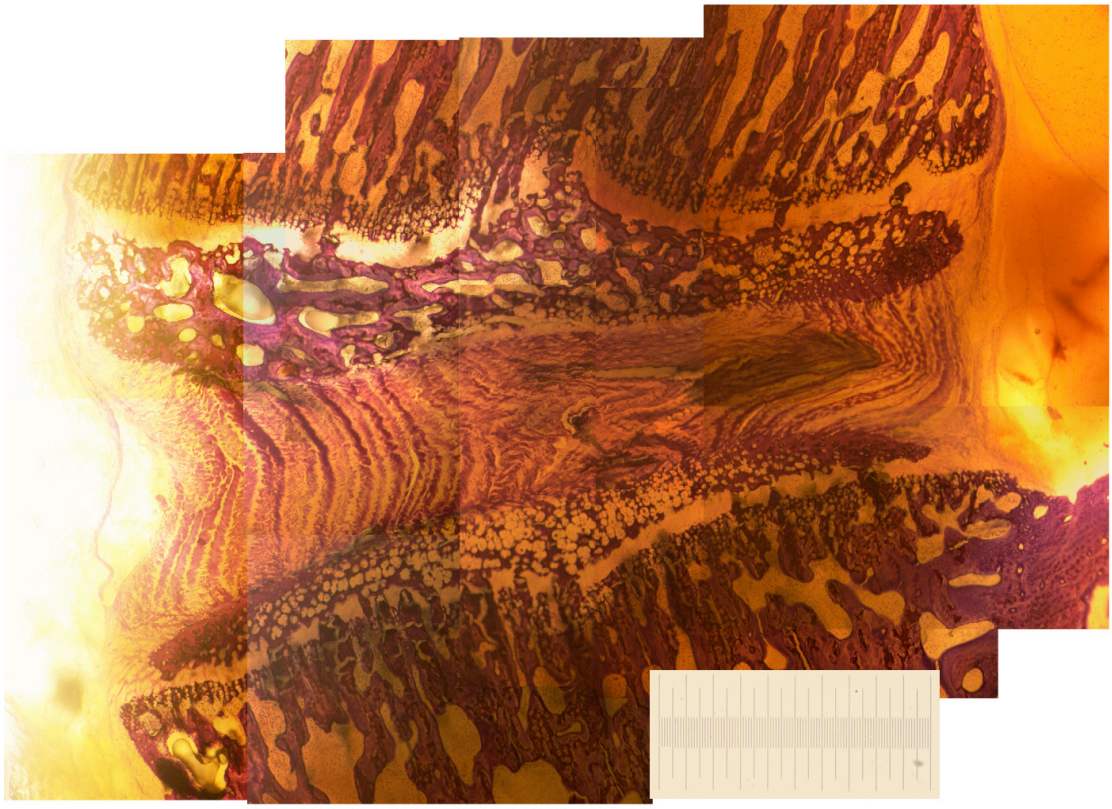

Figure 26 – Rat IVD embedded in PMMA and stained with Toluidine blue

Samples for Figures 26-28 were prepared by embedding the whole spine in PMMA and sectioned into L4-L5 vertebral units. The sections were cut across the mid-sagittal plane, embedded in PMMA, sectioned with a diamond wafering blade, polished to a 3 micron finish, and stained with Toluidine blue. Figures 26-28 were used for thickness and porosity calculations. The variation in endplate thickness can be seen to change across its width. The direction of annuluar fibers can be seen to remain primarily vertical but wrap around and contain the NP. The collapse of the disc due to drying is apparent due to the off-center nature of the NP and the non-concentric vertebrae. There is a clear visible distinction between the upper and lower CE with respect to pore size and distribution. Figure 28 shows great contrast between anatomical features and toluidine blue is an excellent stain for that purpose.

Figure 27 - Rat IVD embedded in PMMA and stained with Massons's Trichrome

The sample in Figure 27 was prepared the same was as the sample in Figure 26 with the exception of the stain. Massons's Trichrome was used in order to try and distinguish muscle, collagen and bone, cytoplasm, and nuclei from each other, but is still sufficient to provide enough contrast for pore size and count in many zones. Similar to the Toluidine Blue stain, the Massons's Trichrome exhibits a large variation between cranial and caudal pore sizes and distributions, the effective height of the IVD based on width, and the changing thickness as a function of location.

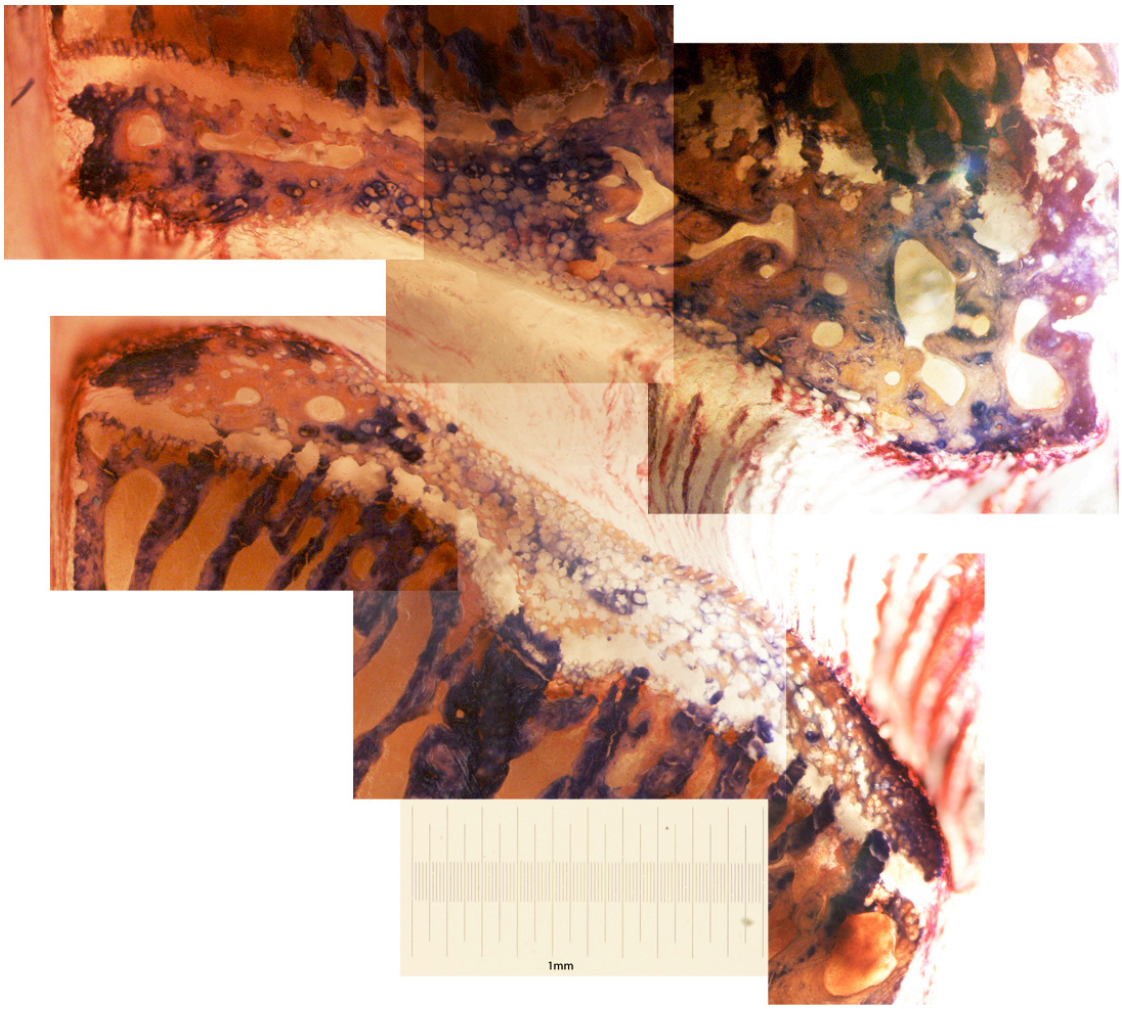

Figure 28 - Rat IVD embedded in PMMA and stained with Massons's Trichrome

Figure 28 is a different sample from Figure 27, but prepared in the same way. This sample highlights the differences between the CE and adjacent bone by contrasting the different collagen densities and motion segment constituents.

	Zone 1	Zone 2	Zone 3	Zone 4	Zone 5
Average Pore Number (Top CE)	17.75	26	30	18.25	13.875
Std Dev	13.5	7.52	17.64	8.43	6.17
Average Pore Number (Bottom CE)	21.875	58.333	43.75	19.444	25
Std Dev	10.88	21.57	10.63	11.41	10.25
Average Pore Size mm^2 (Top CE)	0.0013	0.001	0.0011	0.004	0.0089
Std Dev	0.0008	0.0004	0.0004	0.0041	0.0137
Average Pore Size mm^2 (Bottom CE)	0.00087	0.00086	0.00052	0.000731	0.0006
Std Dev	0.00035	0.000348	0.000043	0.00042	0.00066
Pore Fraction (Top CE)	0.094	0.1552	0.1488	0.1908	0.25
Std Dev	0.0309	0.0623	0.0451	0.0686	0.1117
Pore Fraction (Bottom CE)	0.0799	0.1494	0.1804	0.1843	0.1124
Std Dev	0.025	0.0162	0.0183	0.0497	0.0505

Table 2 - Histological Sample Results
showing the compiled data for all histological samples in this study. Samples were taken from the L4-L5 motion segment of female Sprague-Dawley rats, embedded in PMMA, sectioned, polished, stained using Toluidine Blue or Massons's Trichrome, and imaged with optical microscopy.

Table 2 shows the histological sample results. Pore number, size, and area fraction are computed for the top and bottom CE. There is a clear distinction between both axial and radial location with respect to: pore number, size, and fraction. The standard deviations between these values tended to vary dramatically within the cranial CE and less so within the caudal CE.

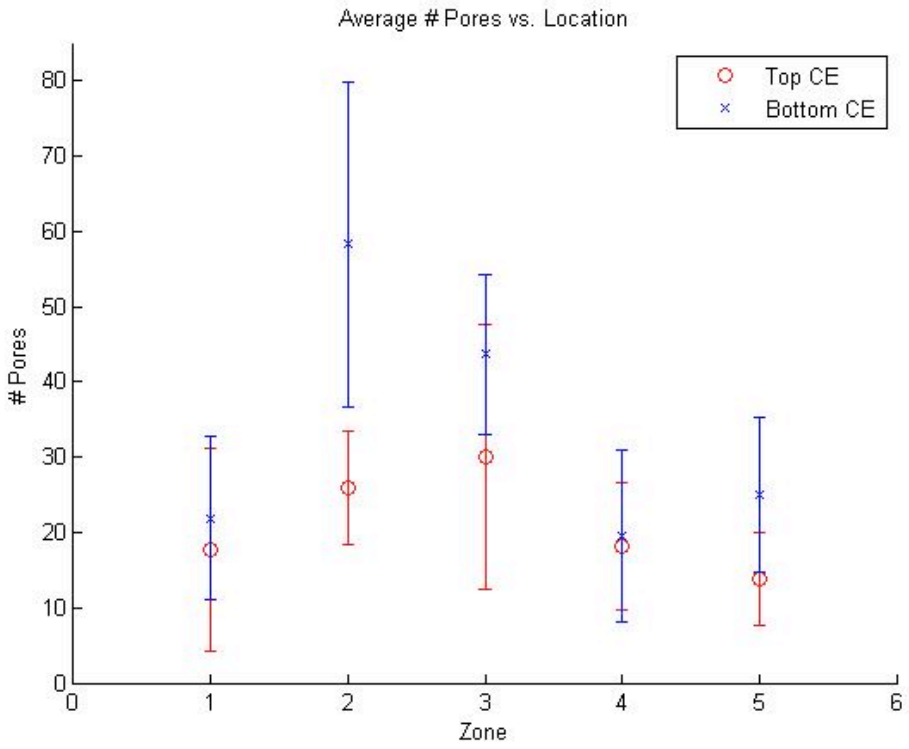

Figure 29 - Average Pore #'s by Zone with Standard Deviations

Graphical representation of the data in Table 2. Figures 26, 27, and 28 are representative images of the sample set and indicate the magnitude of differences between pore properties. Figure 29 illustrates this concept by graphically showing the strong difference between cranial and caudal CE. Furthermore, the distribution of standard deviations is plotted to illustrate the biological variation between samples. Large standard deviations may be reduced with larger sample sizes, but it is more likely that deviations may simply be a inherent to the tissue.

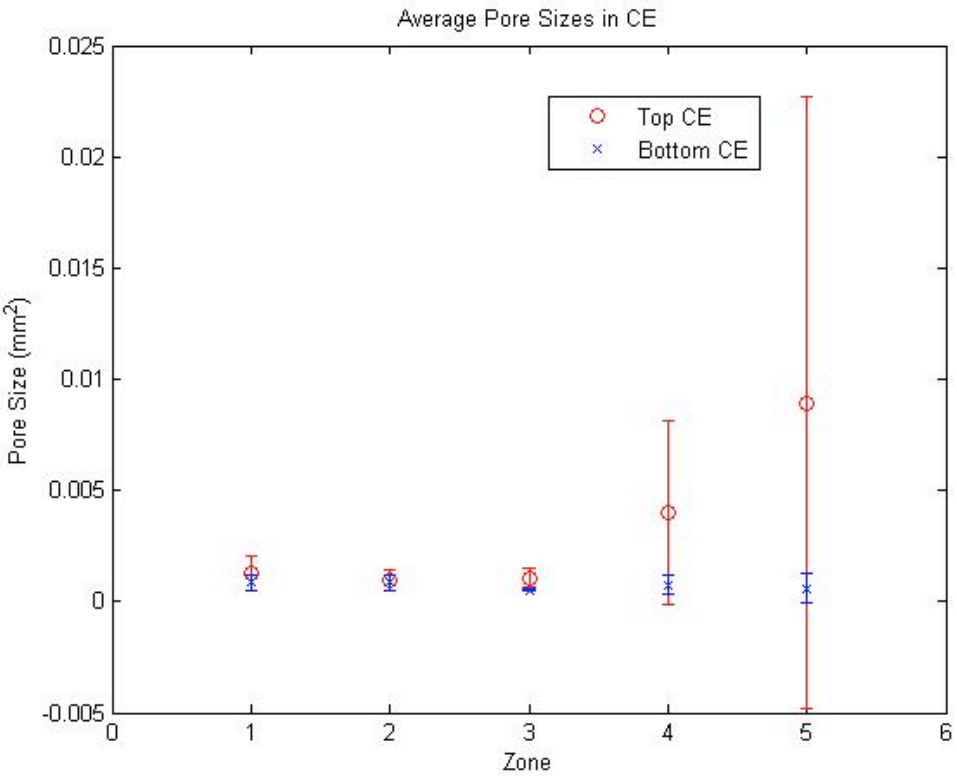

Figure 30 - Average Pore Sizes by Zone with Standard Deviations

Graphical representation of the data in Table 2. Figure 30 illustrates the concept of pore size variability as a function of radial location by graphically showing the strong difference between cranial and caudal CE. Furthermore, the distribution of standard deviations is plotted to illustrate the biological variation between samples. The large standard deviations may indicate that the measurement methods need refinement, or may simply be a biological normality.

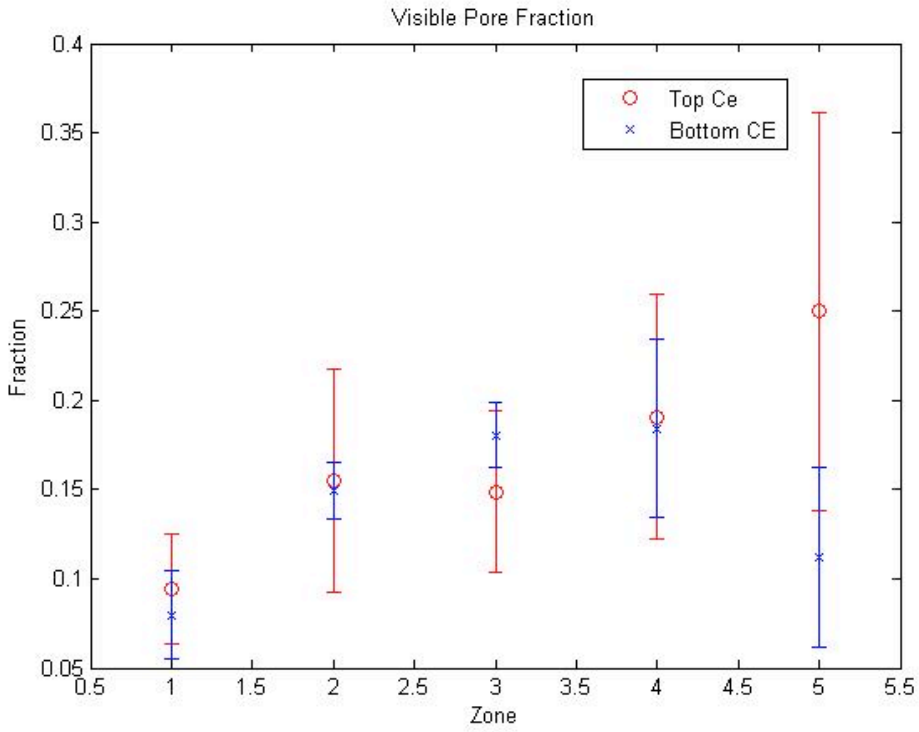

Figure 31 - Pore Fraction by Zone with Standard Deviations

Graphical representation of the data in Table 2. Figure 31 illustrates the differences between the top and bottom CE with respect to pore fraction. Both CE's appear to have similar pore fractions with the exception of Zone 5. Zone 5 in the cranial CE consistently had relatively large pores that contributed to its outlying pore fraction. Anatomically, Zone 5 is distal to the spinal cord, which ay or may not have implications on mechanical loading.

Coefficient of Variance	Zone 1	Zone 2	Zone 3	Zone 4	Zone 5
# Pores (Cranial CE)	0.760	0.289	0.588	0.461	0.444
# Pores (Caudal CE)	0.497	0.369	0.242	0.586	0.410
Pore Size (Cranial CE)	0.615	0.400	0.363	1.025	1.590
Pore Size (Caudal CE)	0.402	0.404	0.082	0.574	1.100
Pore Fraction (Cranial CE)	0.328	0.401	0.303	0.359	0.446
Pore Fraction (Caudal CE)	0.312	0.108	0.101	0.269	0.449

Table 3 – Coefficient of Variance of Pore Data

Table 3 shows the coefficients of variance for pore size, fraction, and number based on zone and anatomical CE location. The values in Table 3 support the understanding that the caudal CE has a numerically smaller spread than its counterpart, the cranial CE.

	Zone 1	Zone 2	Zone 3	Zone 4	Zone 5
Sample 1	0.230	0.178	0.114	0.261	0.414
Sample 2	0.303	0.319	0.389	0.415	0.436
Sample 3	x	x	x	x	x
Sample 4	0.341	0.205	0.170	0.276	0.503
Sample 5	0.248	0.175	0.173	0.407	0.339
Sample 6	0.326	0.241	0.504	0.494	0.921
Sample 7	0.268	0.147	0.226	0.262	0.464
Sample 8	0.261	0.116	0.133	0.342	0.407
Sample 9	0.367	0.157	0.172	0.509	0.934
Sample 10	x	x	x	x	x
Sample 11	0.285	0.272	0.270	0.262	0.511
Mean Thickness (mm)	0.292	0.201	0.239	0.359	0.548
Standard Deviation (mm)	0.046	0.065	0.130	0.101	0.222

Table 4 - Cranial CE Thickness

The cranial CE thickness in Table 4 is shown to have dependence on Zone. The thickness has an upward trend radially outward from the NP with the highest value occurring distal from the spinal cord.

	Zone 1	Zone 2	Zone 3	Zone 4	Zone 5
Sample 1	0.246	0.122	0.117	0.104	0.151
Sample 2	0.152	0.151	0.231	0.182	0.138
Sample 3	x	x	x	x	x
Sample 4	0.391	0.164	0.182	0.201	0.119
Sample 5	0.384	0.238	0.188	0.275	0.267
Sample 6	0.309	0.213	0.283	0.257	0.181
Sample 7	0.350	0.185	0.158	0.193	0.121
Sample 8	0.306	0.151	0.231	0.169	0.112
Sample 9	0.322	0.210	0.184	0.193	0.148
Sample 10	0.349	0.162	0.264	0.382	0.448
`Sample 11	0.379	0.225	0.207	0.246	0.132
Mean Thickness (mm)	0.319	0.182	0.205	0.220	0.182
Standard Deviation (mm)	0.073	0.038	0.050	0.075	0.104

Table 5 - Caudal CE Thickness

The caudal CE thickness in Table 5 is shown to have dependence on Zone. The thickness does not have an upward trend in the outward radial direction like the caudal CE does. The caudal CE has the greatest thickness proximal to the spinal cord and the smallest thickness below the NP and also at the zone most distal to the spinal cord.

5.0 – Discussion

5.1 Sample preparation/imaging methods and evaluation of the methods

5.1.1 SEM Preparation Methods

Many different methods were attempted in order to determine the best approach to gaining reliable porosity data from SEM images. When paired with one of the highest resolutions available today through SEM imaging, the correct sample preparation protocol has the potential to produce unmatched pore counts, sizes, and area fractions.[21] Methods used in research for soft tissue preparation for SEM imaging utilized various chemical and physical means of preparation, and this thesis explored the potential application of these methods to porosity measurements. The physical processes attempted included freeze fracturing, manual separation, and blade cutting. Chemical processes attempted used graded ethanol and/or acetone series, CO_2 critical point drying (CPD), and bleach processing. All possible combinations of physical and chemical processes were attempted with minimal success and low sample yields with respect to porosity measurements. . Freeze fracturing the samples typically produced an irregular surface and caused large amounts of tearing of lamellae but was able to provide very high quality imaging of fiber orientations and lamellae layer observations due to lamellae separation. This is primarily because freeze fracturing exposes tissues along their weakest planes of fracture. Freeze fracturing also proved to be the best method for imaging single fibers (~50nm diameter). This amount of detail improves upon the more common gross anatomical analysis carried out by researchers today.[14] Researchers have had good SEM results when applied to AF fiber orientations and have suggested failure methods based on observation.[21,22] However, this research improves upon that data and adds additional information about not only the AF structure, but also suggests the mechanism with which the IVD is attached to the adjacent vertebral body in the adult rat spine. The phenomenon of stress relief was clearly visible among some samples by

manifesting itself as raised ridges within lamellae and assisted with anatomical confirmation of features.

While not particularly useful for porosity measurements, manual separation and blade cutting provided high quality bone and CE surface images, which led to the additional hypothesis in this thesis, that the soft tissue-bone interface has an attachment mechanism assisted by complex geometry. Bleach processing provided excellent preliminary results, but its inability to provide reliably reproducible data caused it to be abandoned. Choosing between graded ethanol series or acetone to CPD produced similar results with the exception that acetone appeared to remove more of the tissue between layers because the drying was more pronounced. These two methods formed the basis of the chemical approach, and the physical approach was selected based on what feature was intended to be imaged.

No previous research has been published on derived porosity calculations from SEM imaging. Advantages of SEM imaging include 3D rendering of surfaces and depth resolution but come at the cost of artificial artifacts and the inability to resolve the smallest of pores. Fiber bundling and directionality have excellent resolution, even at the smallest of scales, but these scales are too small for quality pore imaging. Therefore, improvement of preparation methods may yield better results, but it is more reasonable to supplement SEM imaging with a more commonly used method (such as histology) for porosity data collection.

The nature of SEM imaging requires adverse conditions to highly hydrated tissue. A vacuum and bombardment of electrons limited the quality yields of samples for analysis. The sample preparation methods require complete dehydration of the tissue; combined with highly hydrated tissue results in large amounts of shrinkage and shape changes. Furthermore, the relatively low electron concentration in the tissue causes the electron beam to dig away at the surface, effectively degrading the sample over time. Even though using SEM for porosity measurements may not be the best method, the results in this research clearly indicate that it is the best method for analysis of surface topography and potential tissue morphology.

5.1.2 Histological Sample Preparation

In order to supplement the limited porosity data provided by SEM imaging while also providing the necessary regional data, various histological methods were probed. It was determined that PMMA embedding would be the best choice due to material and equipment availability, the quality of the prepared samples, and the accuracy of results. The two-dimensional images allowed for measurements of pore number, size, and fraction to be calculated as a function of location. The staining methods were sufficient to perform analysis with confidence due to excellent contrast between anatomical features.

5.2 Attachment Mechanism

Preliminary SEM results revealed a novel functional attachment mechanism between the IVD and adjacent bone that prompted further investigation through histological means.

5.2.1 - 3D Tissue Morphology

Island-like features that were visualized at the surfaces of both the cranial and caudal CE's appeared to form an attachment mechanism between the soft IVD and the hard bone. The modulus discontinuity that exists between bone and cartilage may benefit from such complicated geometry to allow for proper force distribution and to prevent detachment. Imaging from millimeter to micrometer scales shows long range regularity of such "islands." The regularity may in fact be the primary method that the vertebral unit stays together despite a large physiological loading range – at least in the rat. Despite the differences between species, similar results should be expected from both the human and bovine motion segments with the obvious exception of size and the less obvious bipedal-quadruped effects. The human tissue may exhibit smaller property distributions as a function of radius due to the different physiological loading condition. There appears to be no correlation between pore size or distribution of bone and adjacent CE tissue, but there is little data to support this

concept. Further investigation with a substantial data pool would be able to determine if there is a relationship between porosity of the bone and adjacent CE.

5.2.2 – Histological Examination

Histological examination of the aforementioned region show these "islands" traversing the boundary between the endplate and penetrating both the vertebra and endplate. This approach confirms the SEM results while further supporting the idea of "island" features being a mechanism of attachment between the two tissue types. If these features assist in mechanical anchoring, the changing thickness of the CE may also help to keep the IVD centered within the vertebral unit in addition to being the foundation for fluid flow to the region. However, the general contrast to this position is the fact that these "island" features do not appear to exhibit any sort of anatomical change in the radial regions between the AF and NP. Further investigation would need to determine if there is an implication to unchanging CE topology on the aforementioned IVD regions.

5.3 – Data Collection and Analysis

5.3.1 - Volume Fraction Pores

The weight volume fraction of water has been established for the IVD. Gu et al. reports that the weight volume fraction of water ranges from 61-73% depending on age and level of degradation.[15,16] This thesis suggests that SEM imaging visual porosity is unable to account for the entire water fraction and therefore implies that a larger fraction of water must be elsewhere. Increased water fractions must therefore exist within either intrafibrillar space or along irregularly projected 2D planes incapable of being rendered in this study, the latter of which is very unlikely.

5.3.2 – SEM Porosity

The visual area fraction of porosity in the AF can be approximated to be the summation of Figures 24 and (15 or 17) due to large-scale differences. Therefore, the visual AF pore fraction in the axial direction is approximately 30%. Assuming that the AF is about 60% of the total disc, this implies that the NP needs to have a pore fraction in excess of 100%. The implications of these observations are that pore fraction in the radial and/or circumferential directions needs to be in excess of 77% in order to adjust the overall value to that stated in literature or that intrafibrillar porosity contributes significantly to the pore fraction of IVD tissue and is not measurable by means within this study.[15,16] As a result, the SEM data produced in this thesis cannot enable one to deduce absolute porosity from SEM images alone. However, SEM data does provide the necessary information to suggest an anchoring mechanism between tissues.

5.3.3 – Histological Porosity

SEM imaging combined with a histological examination of this tissue presents a new concept of the transition region between similar but different tissue types in the spine. Furthermore, the data obtained from these observations regarding porosity provide perspective and objective information with relevance to permeability of fluid through the vertebral body unit. The number of pores varied from 13-30 per zone in the cranial CE and 19-60 in the caudal CE with the highest numbers just above and below the IVD. This is not a surprising result since research has shown that the highest fluid flux occurs over NP. However, the reasoning for a higher number of pores caudally still proves a mystery. Inspecting the average pore sizes gives more interesting results. Cranially, the average pore size ranges from .001 mm^2 to .0089 mm^2 with coefficients of variations ranging from .363 to 1.59. Caudally, average pore sizes range from only .00052 mm^2 to .00087 mm^2 with coefficients of variation ranging from .082 to 1.1. The reasoning for differences between

cranial and caudal CE pore sizes is unknown. Despite the pore size differences, pore fraction trends were similar to pore number trends, which is the most relevant to permeability models. Cranial CE zones ranged from 9.5-25% (19% excluding Zone 5) and caudal CE zones ranged from 7.5-18.4% pore fraction, a large deviation from expected values in literature.[15,16] Combined with the mathematical method presented herein, the data has the ability to local permeability constants based on concrete observations rather than global assumptions. The discrepancies between observed values of pore number, size, and area fraction conclude that making assumptions about isotropic and homogenous porosity is incorrect and would lead to incorrect simulations.

The fiber connections between lamellae show large amounts of porosity in these regions that suggests high amounts of fluid flow between layers. Relative to the number of fibers within a single layer, the space between layers is possibly an area of mechanical weakness.

5.4 – Limitations

5.4.1 – SEM Limitations

SEM imaging provided minimal quality results due to relatively low sample yields. A large percentage of samples had to either be discarded or ignored due to large amounts of deformation, surface destruction, or inaccurate sectioning. Methods to dehydrate the highly hydrated IVD that were required for SEM imaging were largely problematic despite the numerous approaches. While many preparation methods failed, it was observed that all methods differentially affect the quality of both the final sample and image quality; careful care must therefore be taken with method selection. Successful methods included blade cutting, graded alcohol series, and critical point drying. Acetone immersion also proved to be an effective sample dehydration method. SEM samples were also limited to only the axial plane so other orientations may yield a different 3D composite value for porosity. SEM

observations in this project make clear that there are significant areas of improvement and exploration, primarily regarding developing standards for highly hydrated tissue preparation with SEM. Both chemical and mechanical methods need additional successful experiments to verify their effectiveness.

5.4.2 – Histological Limitations

Histological samples underwent time consuming and multi-step processes so pinning down failure steps proved difficult. Typical histological samples use paraffin embedding, but the nature of bone requires a more robust material, such as PMMA. Staining becomes more difficult with plastic embedded samples, and the hardness differences between materials causes uneven polishing. Histological samples were also limited to only the sagittal plane so other orientations may yield a different 3D composite value for porosity. Despite difficult staining conditions, protocols were quite robust and were still able to produce even and useable staining.

5.5 – Future Work

In future studies, the border transition region between the NP and AF need to be better understood, both mechanically and structurally. The attachment and anchoring mechanism(s) between discontinuous tissue types need extensive research in order to fully understand their function. Observationally, the most common failure method seen in SEM images in this study involved delamination between AF layers. While delamination is not necessarily related to this investigation, the methods applied in this study could possibly be applied to an additional study on the causes and effects of delamination of the AF.

Suggestions to improve histological methods include obtaining ground sections across the various axes of the IVD in order to provide a data pool for local porosity variations. Also, obtaining an embedding medium with mechanical properties between the

soft tissue of the IVD and the mineralized bone should minimize embedding effects, such as modulus mismatch.

Assuming that reliable data can be obtained, additional future work should include development of a large-scale computational model that incorporates local porosity measurements in all body planes of the IVD and CE. Depending on data availability, this model should also include observed mechanical properties within the IVD-vertebrae transition region, which would encompass the concept of the bone-soft tissue interface. Little information is known about this region, and preliminary images produced from this study indicate that there is a strong hierarchical and extremely complex structure present. Also, the derived analytical solution in this thesis relies on constants obtained experimentally for very high water-content agarose gels. These constants need to be calibrated against permeability data for IVD tissue. In order to do this, a permeability study would need to be carried out on IVD tissue for various water contents (or tissue grades) in order to obtain experimentally verified curve fits. With all of the suggested work done, it should be possible to close the gap of understanding between the relationship of the poroelasticity of the IVD and the visual porosity as seen in this study.

6.0 – Conclusions

- Blade cutting combined with ethanol and acetone graded series to critical point drying produced the best SEM results.
- Histological samples provided the most reliable porosity data.
- SEM preparation techniques have large variability in results.
    - Careful attention to preparation method for desired results.
- Dehydrated state porosity is not a true measure of porosity.
    - Measurements need to include intrafibrillar volume.
- The number of pores in the CE is greater above and below the IVD than other locations.
- The average size of pores in the CE is smaller proximal to the spinal cord and increases distally.
    - The cranial CE has a significantly large pore size distribution in the distal 40% while the caudal CE has relatively little change between radial location.
- The pore fraction is greater in the center of the CE's and decreases radially outward.
- The CE thickness may assist in IVD spatial positioning and anchoring.
- The attachment mechanism between the IVD and adjacent vertebrae needs further investigation.

7.0 – References

1. Accadbled, F., Ambard, D., de Gauzy, J.S., Swider, P. (2008). A measurement technique to evaluate the macroscopic permeability of the vertebral end-plate. *Medical Engineering & Physics, 30*, 116-132.

2. Antoniou, J., Demers, C. N., Beaudoin, G., Goswami, T., Mwale, F., Aebi, M., et al. (2004). Apparent diffusion coefficient of intervertebral discs related to matrix composition and integrity. *Magnetic Resonance Imaging, 22*(7), 963-972.

3. Antoniou, J., Goudsouzian, N. M., Heathfield, T. F., Winterbottom, N., Steffen, T., Poole, A. R., et al. (1996). The human lumbar endplate. evidence of changes in biosynthesis and denaturation of the extracellular matrix with growth, maturation, aging, and degeneration. *Spine, 21*(10), 1153-1161.

4. Antoniou, J., Pike, G. B., Steffen, T., Baramki, H., Poole, A. R., Aebi, M., et al. (1998). Quantitative magnetic resonance imaging in the assessment of degenerative disc disease. *Magnetic Resonance in Medicine : Official Journal of the Society of Magnetic Resonance in Medicine / Society of Magnetic Resonance in Medicine, 40*(6), 900-907.

5. Ayotte, D. C., Ito, K., & Tepic, S. (2001). Direction-dependent resistance to flow in the endplate of the intervertebral disc: An ex vivo study. *Journal of Orthopaedic Research : Official Publication of the Orthopaedic Research Society, 19*(6), 1073-1077.

6. Ayers, R. A., Wolford, L. M., Bateman, T. A., Ferguson, V. L., & Simske, S. J. (1999). Quantification of bone ingrowth into porous block hydroxyapatite in humans. *Journal of Biomedical Materials Research, 47*(1), 54-59.

7. Boyde, A., & Firth, E. C. (2004). Articular calcified cartilage canals in the third metacarpal bone of 2-year-old thoroughbred racehorses. *Journal of Anatomy, 205*(6), 491-500.

8. Bishop, J. E., Kiernan, L. A., Montgomery, H. E., Gohlke, P., & McEwan, J. R. (2000). Raised blood pressure, not renin-angiotensin systems, causes cardiac fibrosis in TGR m(Ren2)27 rats. *Cardiovascular Research, 47*(1), 57-67.

9. Department of Physiology, Anatomy, and Genetics, University of Oxford. Intervertebral Disc. In Eurodisc. Retrieved 5/1/09, from http://www.physiol.ox.ac.uk/EURODISC/IntervertebralDisc.png.

10. DM Elliot, & LA Setton. (2000). A linear material model for fiber-induced anisotropy of the anulus fibrosus. *Journal of Biomechanical Engineering, 122*(April), 173-179.

11. DM Elliott, & LA Setton. (2001). Anisotropic and inhomogenous tensile behavior of the human anulus fibrosus: Experimental measurement and material model predictions. *Journal of Biomechanical Engineering, 123*, 256-263.

12. Ferguson, S. J., Ito, K., & Nolte, L. P. (2004). Fluid flow and convective transport of solutes within the intervertebral disc. *Journal of Biomechanics, 37*(2), 213-221.

13. Ganey, T., Libera, J., Moos, V., Alasevic, O., Fritsch, K. G., Meisel, H. J., et al. (2003). Disc chondrocyte transplantation in a canine model: A treatment for degenerated or damaged intervertebral disc. *Spine, 28*(23), 2609-2620.

14. Guerin, H. L., & Elliott, D. M. (2007). Quantifying the contributions of structure to annulus fibrosus mechanical function using a nonlinear, anisotropic, hyperelastic model. *Journal of Orthopaedic Research : Official Publication of the Orthopaedic Research Society, 25*(4), 508-516.

15. Gu,W.Y., Mao,X.G., Foster,R.J., Weidenbaum,M., Mow,V.C., Rawlins,B.A. 1999. The anisotropic hydraulic permeability of human lumbar anulus fibrosus. Influence of age, degeneration, direction, and water content. *Spine*, 24(23), 2449-2455.

16. Gu, W. Y., Yao, H., Huang, C. Y., & Cheung, H. S. (2003). New insight into deformation-dependent hydraulic permeability of gels and cartilage, and dynamic behavior of agarose gels in confined compression. *Journal of Biomechanics, 36*(4), 593-598.

17. Heneghan, P., & Riches, P. E. (2008). Determination of the strain-dependent hydraulic permeability of the compressed bovine nucleus pulposus. *Journal of Biomechanics, 41*(4), 903-906.

18. Holzapfel, G. A., Schulze-Bauer, C. A., Feigl, G., & Regitnig, P. (2005). Single lamellar mechanics of the human lumbar anulus fibrosus. *Biomechanics and Modeling in Mechanobiology, 3*(3), 125-140.

19. Houben, G. B., Drost, M. R., Huyghe, J. M., Janssen, J. D., & Huson, A. (1997). Nonhomogeneous permeability of canine anulus fibrosus. *Spine, 22*(1), 7-16.

20. Huyghe, J.M., Houben, G.B., Drost, M.R., van Donkelaar, C.C. (2003). An Ionised/Non-ionised dual porosity model of intervertebral disc tissue. *Biomechanical Model Mechanobiology, 2*, 3-19.

21. Iatridis, J. C., & ap Gwynn, I. (2004). Mechanisms for mechanical damage in the intervertebral disc annulus fibrosus. *Journal of Biomechanics, 37*(8), 1165-1175.

22. Iatridis, J. C., Kumar, S., Foster, R. J., Weidenbaum, M., & Mow, V. C. (1999). Shear mechanical properties of human lumbar annulus fibrosus. *Journal of Orthopaedic Research : Official Publication of the Orthopaedic Research Society, 17*(5), 732-737.

23. Iatridis, J. C., MacLean, J. J., O'Brien, M., & Stokes, I. A. (2007). Measurements of proteoglycan and water content distribution in human lumbar intervertebral discs. *Spine, 32*(14), 1493-1497.

24. Iatridis, J. C., Setton, L. A., Foster, R. J., Rawlins, B. A., Weidenbaum, M., & Mow, V. C. (1998). Degeneration affects the anisotropic and nonlinear behaviors of human anulus fibrosus in compression. *Journal of Biomechanics, 31*(6), 535-544.

25. Lahr. (2000). Cut Disc. In Ithaca College. Retrieved 5/1/09, from http://www.ithaca.edu/faculty/lahr/LE2000/Back/FinishedPics/JPEGs/CutDisc.jpg.

26. Martinez, J. B., Oloyede, V. O., & Broom, N. D. (1997). Biomechanics of load-bearing of the intervertebral disc: An experimental and finite element model. *Medical Engineering & Physics, 19*(2), 145-156.

27. Moore, R.J. (2000). The vertebral endplate: what do we know?, Review. *European Spine Journal*. 9, 92-96.

28. Moore, R. J. (2006). The vertebral endplate: Disc degeneration, disc regeneration. *European Spine Journal : Official Publication of the European Spine Society, the European Spinal Deformity Society, and the European Section of the Cervical Spine Research Society, 15 Suppl 3*, S333-7.

29. Natarajan, R. N., Ke, J. H., & Andersson, G. B. (1994). A model to study the disc degeneration process. *Spine, 19*(3), 259-265.

30. Oki, S., Matsuda, Y., Shibata, T., Okumura, H., & Desaki, J. (1996). Morphologic differences of the vascular buds in the vertebral endplate: Scanning electron microscopic study. *Spine, 21*(2), 174-177.

31. Perie, D., Korda, D., & Iatridis, J. C. (2005). Confined compression experiments on bovine nucleus pulposus and annulus fibrosus: Sensitivity of the experiment in the determination of compressive modulus and hydraulic permeability. *Journal of Biomechanics, 38*(11), 2164-2171.

32. Power, R. A., Iwaniec, U. T., Magee, K. A., Mitova-Caneva, N. G., & Wronski, T. J. (2004). Basic fibroblast growth factor has rapid bone anabolic effects in ovariectomized rats. *Osteoporosis International : A Journal Established as Result of Cooperation between the European Foundation for Osteoporosis and the National Osteoporosis Foundation of the USA, 15*(9), 716-723.

33. Rao, A. A., & Dumas, G. A. (1991). Influence of material properties on the mechanical behaviour of the L5-S1 intervertebral disc in compression: A nonlinear finite element study. *Journal of Biomedical Engineering, 13*(2), 139-151.

34. Rasband, W.S., ImageJ, U. S. National Institutes of Health, Bethesda, Maryland, USA, http://rsb.info.nih.gov/ij/, 1997-2008.

35. Reid, J. E., Meakin, J. R., Robins, S. P., Skakle, J. M., & Hukins, D. W. (2002). Sheep lumbar intervertebral discs as models for human discs. *Clinical Biomechanics (Bristol, Avon), 17*(4), 312-314.

36. Riches, P. E., Dhillon, N., Lotz, J., Woods, A. W., & McNally, D. S. (2002). The internal mechanics of the intervertebral disc under cyclic loading. *Journal of Biomechanics, 35*(9), 1263-1271.

37. Roberts, S., Urban, J. P., Evans, H., & Eisenstein, S. M. (1996). Transport properties of the human cartilage endplate in relation to its composition and calcification. *Spine, 21*(4), 415-420.

38. Schroeder, Y., Elliott, D. M., Wilson, W., Baaijens, F. P., & Huyghe, J. M. (2008). Experimental and model determination of human intervertebral disc osmoviscoelasticity.

Journal of Orthopaedic Research : Official Publication of the Orthopaedic Research Society, 26(8), 1141-1146.

39. Silva, P., Crozier, S., Veidt, M., & Pearcy, M. J. (2005). An experimental and finite element poroelastic creep response analysis of an intervertebral hydrogel disc model in axial compression. *Journal of Materials Science.Materials in Medicine, 16*(7), 663-669.

40. Smith, L. J., Byers, S., Costi, J. J., & Fazzalari, N. L. (2008). Elastic fibers enhance the mechanical integrity of the human lumbar anulus fibrosus in the radial direction. *Annals of Biomedical Engineering, 36*(2), 214-223.

41. Tanaka, M., Nakahara, S., & Inoue, H. (1993). A pathologic study of discs in the elderly. separation between the cartilaginous endplate and the vertebral body. *Spine, 18*(11), 1456-1462.

42. Travascio, F., & Gu, W. Y. (2007). Anisotropic diffusive transport in annulus fibrosus: Experimental determination of the diffusion tensor by FRAP technique. *Annals of Biomedical Engineering, 35*(10), 1739-1748.

43. Vizza, E., Correr, S., Goranova, V., Heyn, R., Angelucci, P. A., Forleo, R., et al. (1996). The collagen skeleton of the human umbilical cord at term. A scanning electron microscopy study after 2N-NaOH maceration. *Reproduction, Fertility, and Development, 8*(5), 885-894.

44. Wagner, D. R., & Lotz, J. C. (2004). Theoretical model and experimental results for the nonlinear elastic behavior of human annulus fibrosus. *Journal of Orthopaedic Research : Official Publication of the Orthopaedic Research Society, 22*(4), 901-909.

45. Williams, J. R., Natarajan, R. N., & Andersson, G. B. (2007). Inclusion of regional poroelastic material properties better predicts biomechanical behavior of lumbar discs subjected to dynamic loading. *Journal of Biomechanics, 40*(9), 1981-1987.

46. Yu, J., Tirlapur, U., Fairbank, J., Handford, P., Roberts, S., Winlove, C. P., et al. (2007). Microfibrils, elastin fibres and collagen fibres in the human intervertebral disc and bovine tail disc. *Journal of Anatomy, 210*(4), 460-471.

8.0 - Appendix

8.1 – Rat Dissection/Sample Preparation

IVD INVESTIGATION

Rat dissection

TOOLS NEEDED

- Fine tipped scissors
- Bone scissors
- 70% EtOH or 10% bleach for sterilization of surfaces after
- Storage container with moist kim wipes to prevent early dehydration
- Waste container/bag for excess rat tissue
- Gloves

1. Obtain a freshly deceased rat
2. Cut through the skin from the tail to the sternum on the underside of the rat to expose the innards
3. Remove the stomach, large intestine, small intestine, liver, kidneys, and any other organs in the abdominal cavity. Warning: Smelly!
4. Insert scissors (closed) just below the skin at the leg and separate the skin (open scissors) from the muscle tissue, working along the region just above the tail
5. Grab the tail and pull the skin towards the head and off (requires a good amount of force)
6. Use the bone scissors to cut the rat into two sections just above the lowest rib at the spine
7. Discard the upper half as waste
8. Remove the tail and discard as waste
9. Bend the spine near the tail and locate the region where there is no spinal motion. This is the sacrum/ilium. Cut through the middle. Requires a large amount of force. Discard the dorsal section.
10. On the underside, cut through the leg muscle toward the acetabular cup, and cut through it removing the leg
11. Remove the other leg
12. You should now have a section of spine with a fair amount of attached tissue. Wrap the section with a moist kim wipe to prevent dehydration. The next section will describe the cleaning process.

Spine Cleaning Process

TOOLS NEEDED

- Fine tipped scissors, the sharper the better
- Cold plate
- Razor blade or scalpel (either is fine, I used a razor blade it was easier for me)
- Gloves

1. On the anterior of the spine (near the discs) cut lengthwise along the coronal and sagittal planes, removing a "wedge" of tissue
2. Do the same on the mirror plane and again on both back sections
3. Use the scissors to remove the tissue adjacent to the costal processes to expose them
4. With the blade, work around the spine cleaning and removing tissue, careful to note that as more tissue is removed the stability of the spine decreases increasing the risk to the discs. Be careful to maintain straight stability of the spine throughout this process to minimize and/or eliminate damage.
5. If cutting across fresh discs for investigation, use a scalpel blade only as it is much sharper. If freeze fracturing, ignore this step and continue to the freeze fracture section
6. Dispose tissue, gloves, and blades into appropriate containers

Freeze Fracture

TOOLS NEEDED

- 2-methyl butane
- Small Metal container (red bull can with top removed)
- Liquid Nitrogen (approx 1 liter) in a dewar
- Styrofoam box
- Long tweezers
- Hammer
- Scalpel w/ blades
- Scintillation Vials
- Ethanol and/or Acetone (depending on process)
- Bleach (if necessary)
- Gloves
- Liq Nitrogen Gloves
- Safety glasses
- Cold Plate

1. Safety glasses
2. Label scintillation vials, THEN put 70/30 Ethanol and/or Acetone into vials
3. Cool the 70/30 ethanol and/or acetone and/or bleach in the -20C freezer for 30 mins, making sure the liquid does not freeze
4. Prepare scalpel blade, hammer, and cold plate for fracturing
5. Pour the liquid nitrogen into the Styrofoam box (1-2 inches deep)
6. Fill the metal can about halfway with 2-methyl butane
7. Put the spine sections into the 2-methylbutane and quickly place into liquid nitrogen
8. Watch for ice to form in the 2-methylbutane (~2 mins)
9. Remove the spine from the can and quickly place the scalpel on the exposed disc and hit with the hammer. Use a quick and forceful motion.
10. If bleaching, use the following. If not bleaching, skip to 11
    a. Place section into bleach container and agitate for 5 mins
    b. Remove and place back into 2 methylbutane for 2 mins
    c. Remove from 2methylbutane
11. Place into Acetone and/or ethanol series
12. Place into freezer
13. If using 70/30 Ethanol, continue following. If using Acetone, skip to 14
    a. Rotate into 75%, 85%, 90%, 95%, 100% once per day
    b. Can be rotated more often if under time constraint (literature says 3 hrs are necessary)
14. If using Acetone
    a. Leave in freezer for 1 week

Critical Point Drying

TOOLS NEEDED

- 100% Ethanol and/or acetone
- Waste container for fluids

1. Kim Wipes
2. CO_2 dryer

1. Keep tissues in native solvent throughout the process
2. Place samples (in solvent) into chamber and begin substitution process
3. When liquid CO_2 is fully substituted, begin heating to above critical point, careful because of high pressures
4. When above critical point, bleed CO_2 off until dry

Sputter Coating/Mounting

TOOLS NEEDED

- Ag sputter coater
- Colloidal Silver Paste
- Aluminum SEM stubs

1. Mount samples on stubs with colloidal silver paste according to paste directions. Typically requires 30 minutes of dry time before further processing
2. Place samples into chamber and allow to pump down for lat least 10 minutes (to avoid slow pump downs and/or large amounts of out gassing in the SEM
3. Coat the samples with no less than 3nm of Ag and no more than 10nm of Ag. This is to provide conductance for the electron beam. A consistent thickness coating is required for accurate results
4. Ready for imaging

SEM Imaging

TOOLS NEEDED

- Prepared samples
- SEM

1. Follow SEM imaging instructions
2. Use no more than 10kV and no less than 2kV accelerating voltage, 3-4kV is typically optimal for surface imaging

8.2 – Alternate SEM Preparation Method Outcomes

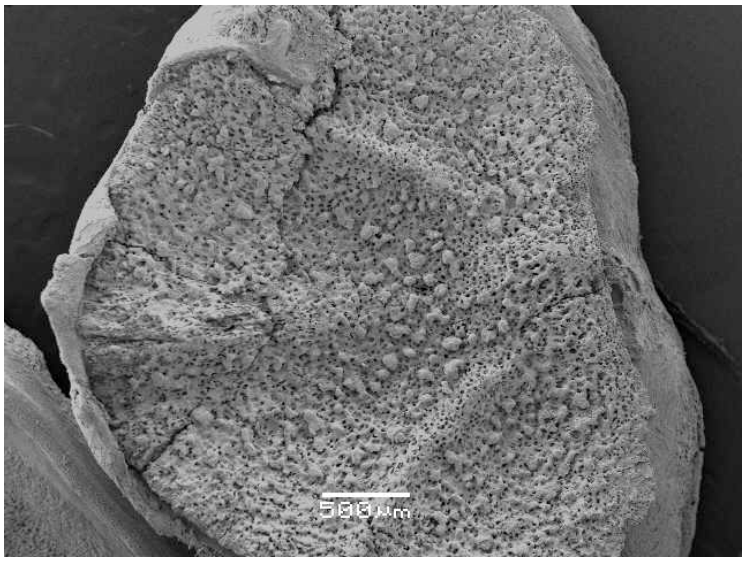

Blade Cut, Bleach, EtOH series

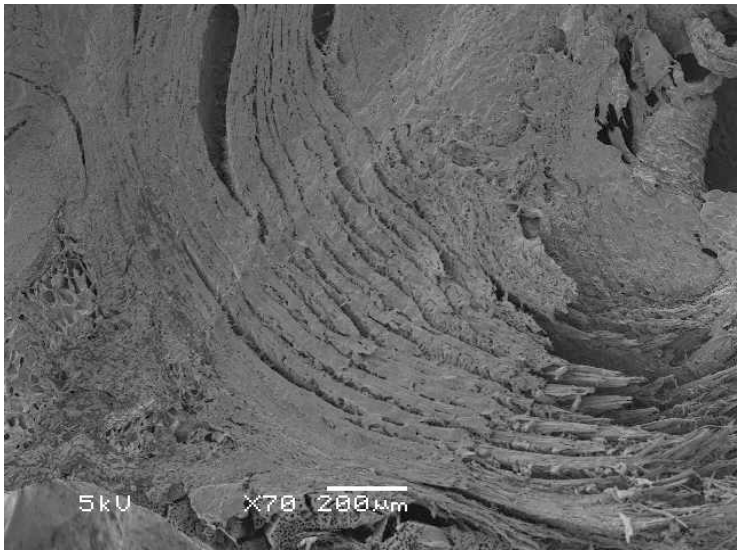

Freeze fracture, Acetone substitution

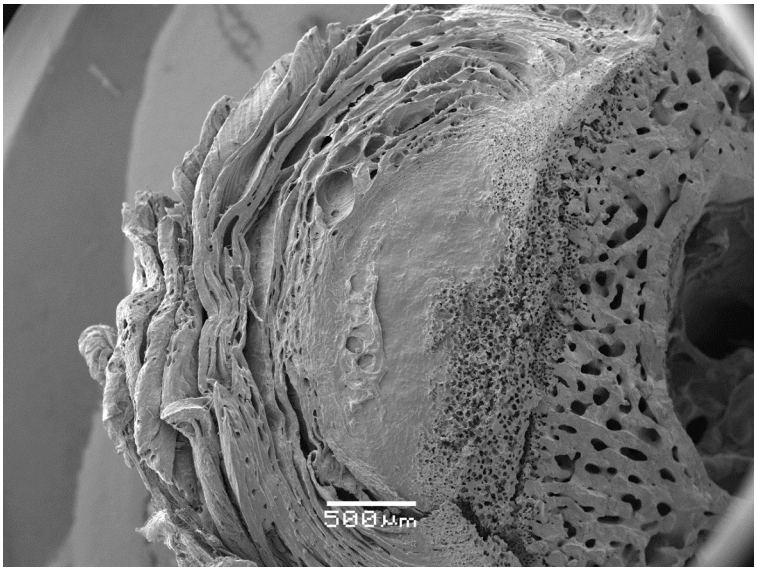

Freeze Fracture, Bleach, Acetone Substitution

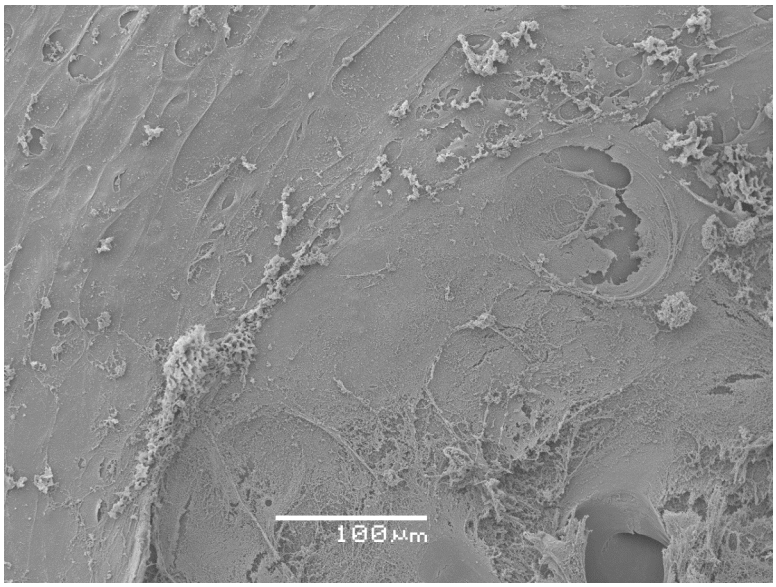

Freeze Fracture, EtOH series (NP-AF border)

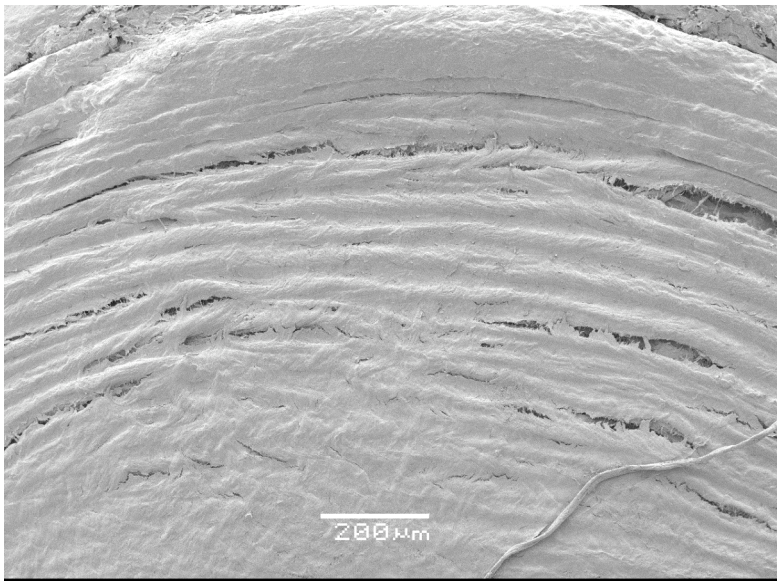

Blade Cut, EtOH series

8.3 – PMMA Embedding Protocol

Samples were embedded in poly (methyl methylacrylate) (PMMA) as follows:

1. Dissect tissue
2. Immerse in 70% ethanol for 24+ hours
3. Position tissue in sectioning geometry using copper wire
4. Immerse in fresh 70% ethanol for 24+ hours
5. Immerse in 80% ethanol for 24+ hours
6. Immerse in 95% ethanol for 24+ hours
7. Immerse in fresh 95% ethanol for 24+ hours
8. Immerse in 100% ethanol for 24+ hours
9. Immerse in fresh 100% ethanol for 24+ hours
10. Clear with 100% acetone for 24+ hours
11. Mix monomer #1 as follows
    a. At room temperature for 2 hours or until clear
        i. 1 gm benzoyl peroxide
        ii. 100 ml MMA
        iii. 5 ml dibutyl pthalate
12. Immerse samples in monomer #1 for 24 hours – draw vacuum
13. Mix monomer #2 as follows
    a. At room temperature for no more than 10 hours (until clear)
        i. 1 gm benzoyl peroxide
        ii. 100 ml MMA
        iii. 5 ml dibutyl pthalate
        iv. 5 gm PMMA
14. Immerse samples in monomer #2 for 24 hours – draw vacuum
15. Repeat steps 13-14 – draw vacuum
16. Mix monomer #3 as follows
    a. Fresh monomer #3 is mixed and stored overnight – don't mix for over 24 hours
        i. 1 gm benzoyl peroxide
        ii. 100 ml MMA
        iii. 5 ml dibutyl pthalate
        iv. 15 gm PMMA
17. Specimens are oriented in containers and placed in water bath set to 37^{o}C overnight.

8.4 – Toluidine Blue Staining Protocol

With a smooth clean surface of tissue embedded in PMMA or similar medium

1. Etch with .1% formic acid for 3 minutes
2. Rinse tap water
3. Immerse in 20% methanol for 120 minutes
4. Rinse tap water
5. Stained with toluidine blue solution for 2 minutes
    a. 1 g toluidine blue
    b. 1 g sodium tetraborate
    c. 100 g distilled water
    d. Filter twice before use
6. Rinse distilled water
7. Blot dry